FACULTY OF SCIENCE AND TECHNOLOGY

MASTER THESIS

Study programme / specialisation:

Engineering Structures and Materials, specialization within Renewable Energy.

The spring semester, 2022

Open

Author:

Abderrafie DARHOUANE

Abdarhouane

(Signature author)

Course coordinator: Dimitrios Pavlou.

Supervisor(s): Knut Erik Teigen Giljarhus.

Thesis title:

Numerical investigation of wind load acting on a ground fixed solar panel.

Credits (ECTS): 30

Keywords:

Solar panels, Computational fluid dynamic analysis, Wind loads, RANS, Atmospheric Boundary Layer, Drag and lift coefficient, Surface pressure.

Pages: 59

+ appendix: 1

Stavanger, 15th of June 2022

Master of Science in Engineering Structures and Materials

Numerical investigation of wind load acting on a ground fixed solar panel.

Submitted by:

Abderrafie DARHOUANE

Supervisor:

Dr. Knut Erik Giljarhus

Submission date:

June 15th, 2022

Faculty of Science and Technology

Department of Mechanical and Structural Engineering and Materials Science.

Preface

I would like to thank all people who contributed to the success of my thesis and who helped me during the writing of this report especially my parents who supported me and contributed to the success of this work.

I would like to thank Mr. Knut Erik Teigen Giljarhus, associate professor within the field of computational fluid dynamics at the University of Stavanger and my thesis supervisor for his considerable advices, availability and his expertise's sharing on a daily basis, which enable me to carry out this work.

I also dedicate this work, to my parents who supported, encouraged and advised me during these years of study. May they find here the testimony of my deep gratitude.
To my brothers, my grandparents and those who shared with me all the emotional moments during the realization of this work. They have warmly supported and encouraged me throughout my journey.

To my family, my relatives and those who give me love and vivacity. To all my friends who always encouraged me, and to whom I wish more success.

To all those I love.

Thank you for your support!

June 2022, Stavanger, Norway
Abderrafie DARHOUANE

Abstract

The photovoltaic panels are one of the most important components to achieve the goal of decarbonization of the electricity and energy sectors. With the use of ANSYS Fluent, an advanced computational fluid dynamics (CFD) tool, the effects of tilt angles and wind directions on solar panels' force coefficients (notably drag and lift) are investigated. After reading the report, readers will gain a better understanding of the aerodynamic behavior of a single and two separate ground fixed solar panels as well as a consecutive array by varying the tilt angles and wind directions, in addition to being able to set up the same case using ANSYS Fluent software. The simulations are carried out on several meshes and solved using a three-dimensional steady-state $k - \omega$ shear stress transport Reynolds Averaged Navier-Stokes (RANS) turbulence model. The coefficients from three tilt angles (15°, 25°, and 45°) and four different wind directions (0°, 45°,135°, and 185°) will be compared to Jubayer's experimental results (Jubayer, C. M. (2014)). The simulations were run using a Reynolds number of $2.13x10^6$ for a stand-alone solar panel, and $2.96x10^6$ for wind effects on consecutive arrays. Otherwise, this study compares steady-state and transient flow simulations, where the resulting coefficients were in a respectable correspondence with the experimental results.

Keywords: Solar panels, Computational fluid dynamic analysis, Wind loads, RANS, Atmospheric Boundary Layer, Drag and lift coefficient, Surface pressure.

Nomenclature

Abbreviations

ABL	Atmospheric Boundary Layer.
ASCE	American Society of Civil Engineers.
BIPV	Building Integrated Photovoltaics.
CFD	Computational Fluid Dynamics.
COST	European Cooperation in Science and Technology.
ESDU	Engineering Sciences Data Unit.
PV	Photovoltaic.
PhD	Doctor of Philosophy.
PISO	Pressure Implicit with Splitting of Operators.
RANS	Reynolds-Averaged Navier-Stokes.
SST	Shear Stress Transport.
TKE	Turbulence Kinetic Energy.
TI	Turbulence Intensity.
UDF	User-Defined Function.

Greek and Latin letters

ρ	Density of Air.
H	Panel's height.
L	Panel's length.
θ	Panel tilt angle.
G_k	Production of turbulence kinetic energy.
μt	Turbulent viscosity.
ε	Rate of dissipation of turbulence energy.
k	Turbulent kinetic energy.
νt	Turbulent kinematic viscosity.
Re	Reynold's number.

I	Turbulence intensity.
$\mathrm{C}f$	Friction coefficient.
Y_k	Dissipation of k.
S_k	User-defined source term.
S	Strain rate magnitude.
$\mathit{\Gamma}_k$	Effective diffusivity of k.
σ_k	Turbulent Prandtl number for k.
F	Blending functions.
α	Volume fraction.
P	Pressure.
W	Width of the panel.
A	Surface area of the panel.
δ	Wind direction.
ω	Specific dissipation rate.
μ	Dynamic viscosity.
$\mathrm{C}p$	Pressure Coefficient.
$\mathrm{C}\ell$	Lift Coefficient.
$\mathrm{C}d$	Drag Coefficient.
$C\mu$	Turbulence model constant.
v	Kinematic viscosity.
x	x-coordinate.
Y_ω	Dissipation of ω.
S_ω	User-defined source term.
D_ω	Cross-diffusion term.
$\mathit{\Gamma}_\omega$	Effective diffusivity of ω.
σ_ω	Turbulent Prandtl number for ω.
G_ω	Generation of ω.
κ	Von Karman’s constant.

This page was intentionally left blank

Table of Contents

List of Figures

List of Tables

Chapter. 1

I. Introduction

1.1 General introduction

As the world population expands, the global energy’s demand is set to increase promptly, and as emissions from fossil fuels, oil, coal, and gas make a dire change in the earth’s climate, the individuals think twice about how to supply greener sustainable, and renewable energy sources. The sun is the primary source of all energy available on our planet, the proper use of this natural resource meets the basic energy needs of humans (Coley, 2011).

Solar photovoltaic model is a way of producing electricity out of radiation coming from the sun, a climate-friendly technology which converts the photons into electricity with a lower production cost, less maintenance, and at variance scales (Coley, 2011). The majority of PV technology are used in low-power devices and technologies, including pocket calculators, small pumps, outside lamps, or telecommunications systems in remote locations. Otherwise, we have also begun to use this technology on a larger scale through the heating of water reservoirs, power generation, and building-mounted photovoltaic energy (Coley, 2011). The photovoltaic panels can be installed on the roof and building envelope, known as building-integrated photovoltaic (BIPV), or on the ground. PV solar farms are developed in open terrain, with a set of rows of ground-mounted panels separated by well-calculated distances to avoid shadows from the panels and the surroundings.

Over the past decade, the solar panels have had a high installed capacity with an expectation of up to 228 GW in 2022 (BloombergNEF, 2022). These solar plans require a safe implementation, with a robust and powerful support design to resist natural disasters, such as sand encroachment and wind gusts. The aerodynamic section has been the subject of numerous studies and research on the effects of wind on single and consecutive solar panels. Plenty of investigations have been developed for both stand-alone and array configurations, with wind tunnel testing being the main used method to study this kind of subject, among these researches (Aly & Bitsuamlak, 2013),(Jubayer, 2014) (Shademan, Barron, Balachandar, & Hangan, 2014), Although, fewer studies were performed by the use of computational fluid dynamics, with limited tilt angles and wind directions (Jubayer, 2014). In general, OpenFoam was the fundamental computational software used for these researches. However, ANSYS Fluent will be employed for this work using a $k - \omega$ shear stress transport (SST) turbulence model, with multiple case studies. The reason for selecting different software is owing to the limited time frame schemed for the thesis, as several scenarios have been simulated and compared to the previous research. As shown in Figure 1, the given study explores the behavior of pressure, lift, and drag coefficients on panel surfaces for a stand-alone panel, five consecutive arrays, and two separated panels.

The placement of solar panels leans on the supporting columns, wind direction, and tilt angles, and must be properly taught. As a result, the more exposed the surface to the wind, the more likely an accident occurs. The relocation of the solar panel due to wind force applied from the solar arrays’ backside is seen in Figure 2.

Figure 1. "Solar panel farm in central solar dos Barros", by Mariana Proença. (Proença, 2018).

Figure 2. "Solar panel modules displaced by wind force". Credit: CASE Foresnics.(Foresnics, 2015).

1.2 Outline and objectives

The contribution of this work is divided into three parts. First, the wind load acting on a ground-mounted solar panel is discussed and analyzed, where the panel is assessed for three different tilt angles (15°,25°,45°) and wind directions (0°,45°,135°,180°), as well as simulating various grids, to verify how the grid affects the results. Otherwise, this chapter contains a comparison of steady-state and transient flows at a tilt angle of 25° (Jubayer, 2014). In the second section, the influence of two solar modules separated by four different gap distances is investigated. The final chapter examines the impact of inclination angles and wind direction on five consecutive arrays of ground-mounted solar panels.

The main goal of this aerodynamic study is to enhance the aerodynamic characteristics and maneuverability of solar panels in open terrain. From several perspectives, this report details the validation of pressure, drag and lift coefficients using Computational Fluid Dynamics (CFD). Additionally, a three-dimensional setup will be modeled using the Shear Stress Transport (SST) $k - \omega$ turbulence model, as it has an adequate accuracy of flow separations and stress gradients. This thesis also aims to assess the grid sensitivity of a ground-mounted solar panel and to compare the findings for various mesh elements. Furthermore, instead of the transient model relied on by previous studies, this report uses the steady-state model to gain insights from the existing literature, particularly in the geometrical domain.

Chapter. 2

II. Theory

2.1 Aerodynamic loads

This study considers three fundamental coefficients. Equations 1 and 2 are used to compute the two most important aerodynamic coefficients: drag and lift (Karimirad & Moan, 2012). The pressure distribution on the panel surface is also carried out based on the pressure coefficient specified by Equation 3. As a result of the simulation, the following coefficient parameters are obtained (Jubayer, 2014):

- Drag coefficient C_d

$$C_d = \frac{2F_d}{A\rho u^2} \qquad \text{Eq. 2.1.1}$$

- Lift coefficient C_ℓ

$$C_\ell = \frac{2F_l}{A\rho u^2} \qquad \text{Eq. 2.1.2}$$

- Pressure coefficient C_p

$$C_p = \frac{2\Delta p}{\rho u^2} \qquad \text{Eq. 2.1.3}$$

Where: F_d is the drag force, F_l the lift forces, A is the area of the panel, ρ is the fluid's density, v is the overall velocity, and Δp is the pressure difference.

The Reynolds number is defined as:

$$Re_L = \frac{\rho u L}{\mu} = \frac{uL}{v} \qquad \text{Eq. 2.1.4}$$

Here, v is the kinematic viscosity, ρ is the density, L is the length of the panel and u is the velocity.

There are six faces of a solar panel, but this study focuses on the upper and lower surfaces exposed to the incoming wind from various wind directions, as shown in Figure 3.

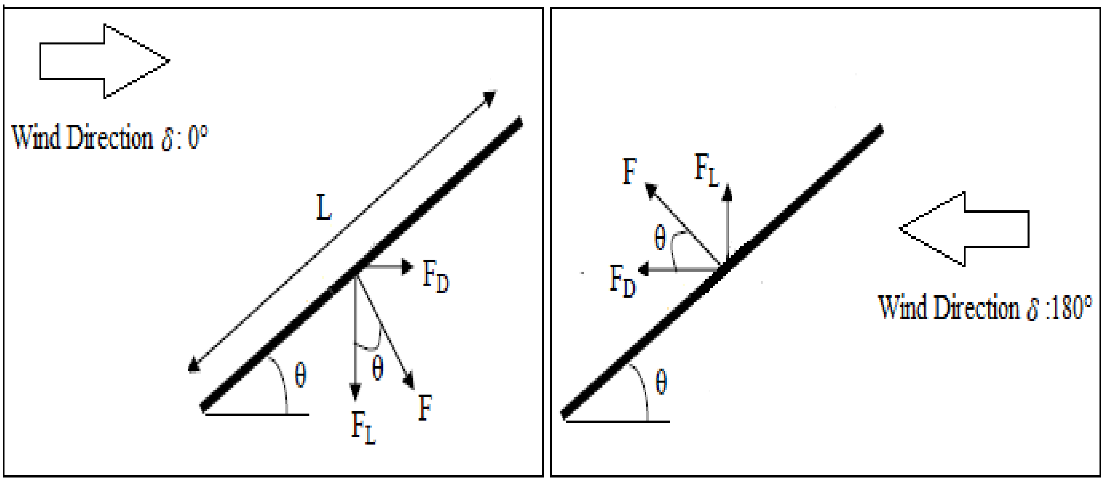

Figure 3. Aerodynamic forces at 0°,180° wind direction on a tilted plate.(Jubayer, 2014)

2.2 Computational fluid dynamics

2.2.1 *K ω SST-RANS model*

The Reynolds-Averaged Navier– Stokes (RANS) equation is one of the turbulence models, which severely simplified the equations using the mean flow and time-averaged properties of the flow, basically mean pressures, mean velocities, and mean stresses (Versteeg & Malalasekera, 2007). An additional component known as the Reynold stress appears in the time-averaged flow equation as a result of the interactions among multiple turbulent fluctuations. This method has been at the core of engineering flow calculations for the past three decades, as the computing resources required for reasonably accurate flow calculations are modest (Versteeg & Malalasekera, 2007).

The SST $k - \omega$ model has a suitable estimation of the flow separation and stress gradients of the two transport equations. This is called the Menter SST $k - \omega$, a transformation of the k– ε model into a k– ω model in the near-wall region and the standard k– ε model in the fully turbulent region far from the wall (Menter, 1992, 1997). It was introduced in 1994 by F.R. Menter to overcome the freestream sensitivity of the $k - \omega$ model and improve its performance in the near wall boundary layer with adversepressure gradients. Both the Reynolds stress computation and the k-equation are similar to Wilcox's original k– ω model, although the ε-equation is transformed into an ω-equation by substituting $\varepsilon = k * \omega$ (Versteeg & Malalasekera, 2007).

The SST k– ω model of Menter et al. (2003) uses the following turbulent kinetic energy equations. (Fluent, 2013):

$$\frac{\partial}{\partial t}(\rho k) + \frac{\partial}{\partial x_{\mathrm{i}}}(\rho k u_{\mathrm{i}}) = \frac{\partial}{\partial x_j}\left(\Gamma_k \frac{\partial k}{\partial x_j}\right) + G_k - Y_k + S_k$$

Eq. 2.2.1.1

$$\frac{\partial}{\partial t}(\rho \omega) + \frac{\partial}{\partial x_j}(\rho \omega u_j) = \frac{\partial}{\partial x_j}\left(\Gamma_\omega \frac{\partial \omega}{\partial x_j}\right) + G_\omega - Y_\omega + D_\omega + S$$

Eq. 2.2.1.2

The effective diffusivity for k and ω are:

$$\Gamma_k = \mu + \frac{\mu_t}{\sigma_k}$$

Eq. 2.2.1.3

$$\Gamma_\omega = \mu + \frac{\mu_t}{\sigma_\omega}$$

Eq. 2.2.1.4

The turbulent viscosity μ_t , the turbulent Prandtl numbers σ_k and σ_ω are equal to:

$$\mu_t = \frac{\rho k}{\omega} \frac{1}{\max\left\{\frac{1}{\alpha^*}, \frac{S\,F_2}{a_1 \omega}\right\}}$$

Eq. 2.2.1.5

$$\sigma_\omega = \frac{1}{\frac{F_1}{\sigma_{\omega,1}} + \frac{(1 - F_1)}{\sigma_{\omega,2}}}$$

Eq. 2.2.1.6

$$\sigma_k = \frac{1}{\frac{\mathrm{F}_1}{\sigma_{k,1}} + \frac{(1-\mathrm{F}_1)}{\sigma_{k,2}}} \qquad \text{Eq. 2.2.1.7}$$

The high-Reynolds-number gives a coefficient of damping $\alpha^* = 1$.

S is the strain rate magnitude and F_1 , F_2 are the blending functions computed as follows:

$$F_1 = \tanh(\Phi_1{}^4) \qquad \text{Eq. 2.2.1.8}$$

$$\Phi_1 = \min\left\{\max\left\{\frac{\sqrt{k}}{0.09\omega y}, \frac{500\mu}{\rho\omega y^2}\right\}, \frac{4\rho k}{\sigma_{\omega,2} D_\omega{}^+ y^2}\right\} \qquad \text{Eq. 2.2.1.9}$$

The term y represents the distance to the following surface.

$$D_\omega{}^+ = \max\left\{2\rho\frac{1}{\sigma_{\omega,2}}\frac{1}{\omega}\frac{\partial k}{\partial x_j}\frac{\partial \omega}{\partial x_j}, 10^{-10}\right\} \qquad \text{Eq. 2.2.1.10}$$

$$F_2 = \tanh(\Phi_2{}^4) \qquad \text{Eq. 2.2.1.11}$$

$$\Phi_2 = \max\left\{2\frac{\sqrt{k}}{0.09\omega y}, \frac{500\mu}{\rho\omega y^2}\right\} \qquad \text{Eq. 2.2.1.12}$$

The production G_ω term is given by

$$G_\omega = \frac{\alpha}{\nu_t} G_k \qquad \text{Eq. 2.2.1.13}$$

The constant term α_∞ in the SST *k-ω* model is:

$$\alpha_\infty = F_1\,\alpha_{\infty,1} + (1 - F_1)\alpha_{\infty,2} \qquad \text{Eq. 2.2.1.14}$$

Where,

$$\alpha_{\infty,1} = \frac{\beta_{i,1}}{\beta^*_\infty} - \frac{\kappa^2}{\sigma_{\mathrm{w}.1}\sqrt{\beta^*_\infty}} \qquad \text{Eq. 2.2.1.15}$$

$$\alpha_{\infty,2} = \frac{\beta_{i,2}}{\beta^*_\infty} - \frac{\kappa^2}{\sigma_{\mathrm{w}.2}\sqrt{\beta^*_\infty}} \qquad \text{Eq. 2.2.1.16}$$

Von Karman’s constant κ equal to 0.41

2.2.2 Atmospheric Boundary Layers

The Atmospheric Boundary Layer (ABL) is located in the lower zone of the troposphere, where the atmosphere is impacted by the physical quantities of the ground, such as temperature and wind (Spiridonov & Ćurić, 2021). Velocity, turbulent kinetic energy, and turbulent dissipation profile at each height of the inlet boundary are interpreted using a user-defined function based on the following equations (Blocken, Stathopoulos, & Carmeliet, 2007):

- Velocity profile $u(z)$:

$$u(z) = \frac{u^*}{\kappa} \ln\left(\frac{z + z_o}{z_o}\right) \qquad \text{Eq. 2.2.2.1}$$

$$u^* = \frac{u_{ref}\kappa}{log\left(\frac{z_{ref}+z_0}{z_0}\right)} \qquad \text{Eq. 2.2.2.2}$$

- Turbulent kinetic energy profile $k(z)$:

$$k(z) = \frac{{u^*}^2}{\sqrt{c_\mu}} \qquad \text{Eq. 2.2.2.3}$$

- Turbulent dissipation rate $\epsilon(z)$:

$$\epsilon(z) = \frac{{u^*}^3}{\kappa(z + z_o)} \qquad \text{Eq.2.2.2.4}$$

Where,
$u^*$is the friction velocity, z is the height coordinate, $c_\mu$is the model constant of the standard k-ε model, and the Von Karman’s constant noted by κ.

2.2.3 Implementation of k-ω SST model in ANSYS

In the present thesis, ANSYS simulation software has been employed to analyze and visualize the results. The fluid flow analysis system is known as (FLUENT), where geometries are imported or created using DesignModeler and meshed by the ANSYS meshing system. The viscous model and boundary conditions are defined in the setup section of the next step. In addition, the solution unit of the residual monitor specifies the solution method and absolute criteria. Finally, ANSYS CFD-Post displays the finding results, including contours and streamlines (Fluent, 2009).

As a low Reynolds turbulence model without any further damping effect, the k-ω SST model is better utilized for problems involving external aerodynamics. This model is well suited for simulating viscous sub-layer flow. It performs well in adverse pressure gradients and flow separations (Online, 2014).

The following table shows the SST *k-ω* model constants employed in the current analysis.

Table 1. Constants for k-ω SST Model.

β^*_∞	a_1	$\beta_{i,1}$	$\beta_{i,2}$	$\sigma_{k,1}$	$\sigma_{k,2}$	$\sigma_{\mathrm{w}.1}$	$\sigma_{\mathrm{w}.2}$	c_1	α^*_∞	α_∞
0.04	0.31	0.032	0.0368	0.85034	0.38	0.44	0.85616	10	1	0.5

Chapter. 3

III. Analysis of wind load acting on a ground fixed solar panel

The solar panels examined in our study contain 4 rows by 6 columns of each model size (1.2m x 0.6m). The dimension of the entire single panel is 2.48m (B) x 7.2 m (W), with a minor thickness of 0.07m, as shown in Figures 5 and 6**.** The wind direction δ is chosen based on the x component, while the tilt angle θ indicates how far the panel is angled from the ground (XZ plane).

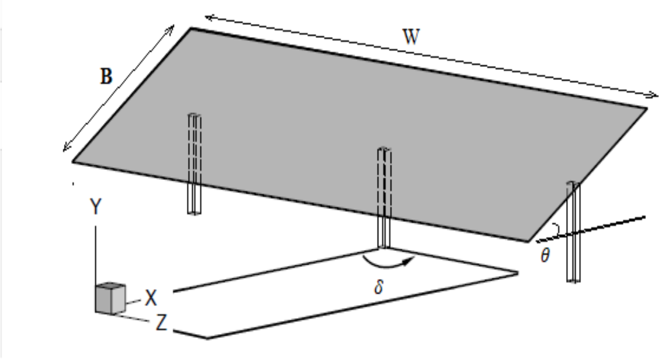

Figure 4. Tilt angle θ – Wind direction δ. (Jubayer, 2014)

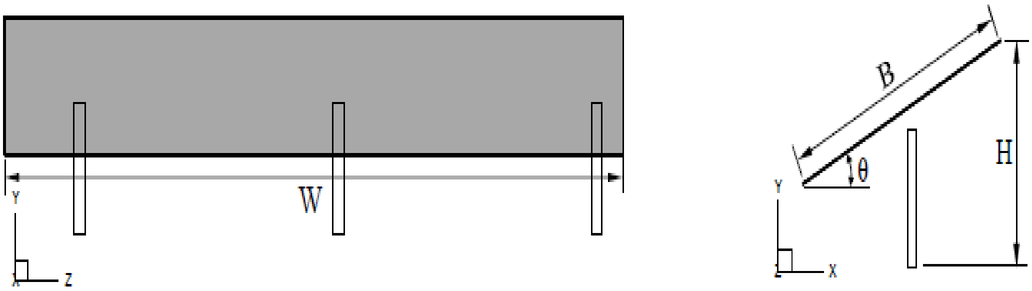

(a) (b)

Figure 5. The stand-alone PV system (a) Front view (b) Side view. (Jubayer, 2014)

3.1 Dimensions of the domain

The grid domain dimension given in this study is based on the specific recommendations of the COST guidelines, in which the domain dimensions are calculated from the object height (Franke, Hellsten, Schlunzen, & Carissimo, 2011). This distance is estimated from the ground to the highest point of the photovoltaic panel for the stand-alone PV panel (Figure 5 (b)). The top wall must be at least 5H above the highest part of the solar panel, which means that the height of the computational domain is around 6H. The distance from the inlet to the front section of the object is fixed at 5H. However, 15H distance of the air domain is considered between the highest point of the panel and the outlet in order to observe the wake region of the flow (Franke et al., 2011). Furthermore, the lateral extension of the domain of 21.4H is chosen from both of the domain's symmetric walls. The overall domain size of 21.4H x 6H x 24.2H is shown in Figure 6.

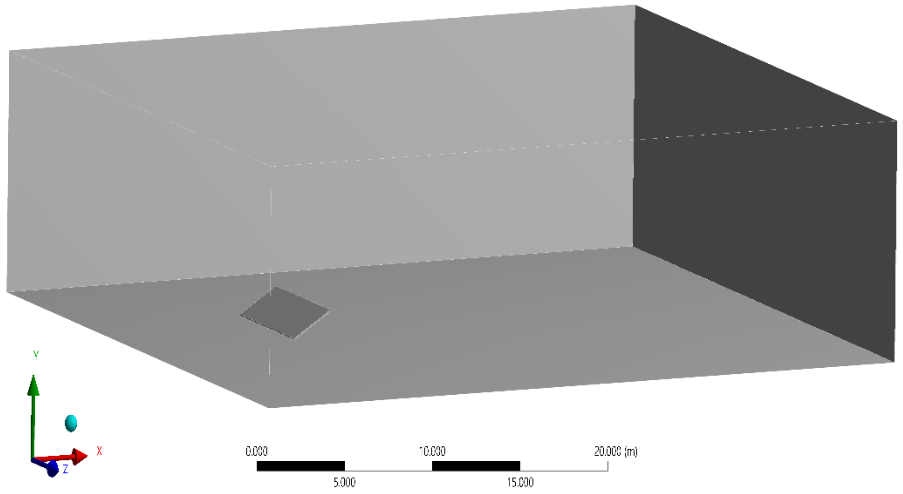

Figure 6. Computational domain of stand-alone PV panel.

3.2 Computational setup

In this chapter, we will use the ANSYS Meshing system to generate elements with four grid sizes 250473, 601387, 1663163, and 4325448. The main goal is to compare the results obtained in each case and analyse the grid sensitivity of the model. The Reynolds number was chosen to 2.13×10^6, and y^+ was set to 1. The next sub-sections will go into further specifics details.

3.2.1 Boundary Conditions

The same boundary conditions were used throughout this thesis. The computational domain consists of six faces, the two faces on the side boundaries are considered as symmetry. The bottom boundary is settled as a no-slip rough wall with an aerodynamic roughness of 0.03 m for exposure in open terrain. The inlet boundary velocity is based on an interpreted user-defined function to create the Atmospheric Boundary Layer (ABL), where the wind speed profile is set to 26 m/s at an altitude of 10 m as employed by (Jubayer, 2014).

Additionally, the upper and lower surfaces of the panel are chosen as no-slip walls. The velocity value is selected at the top of the domain as a constant speed over the entire domain, based on the ABL profile. It is also necessary to neglect the pressure difference at the outlet face as the solar panel has less volume compared to the flow domain. Figure 7 shows the curves of inlet velocity and turbulence intensity as a function of the computational domain height.

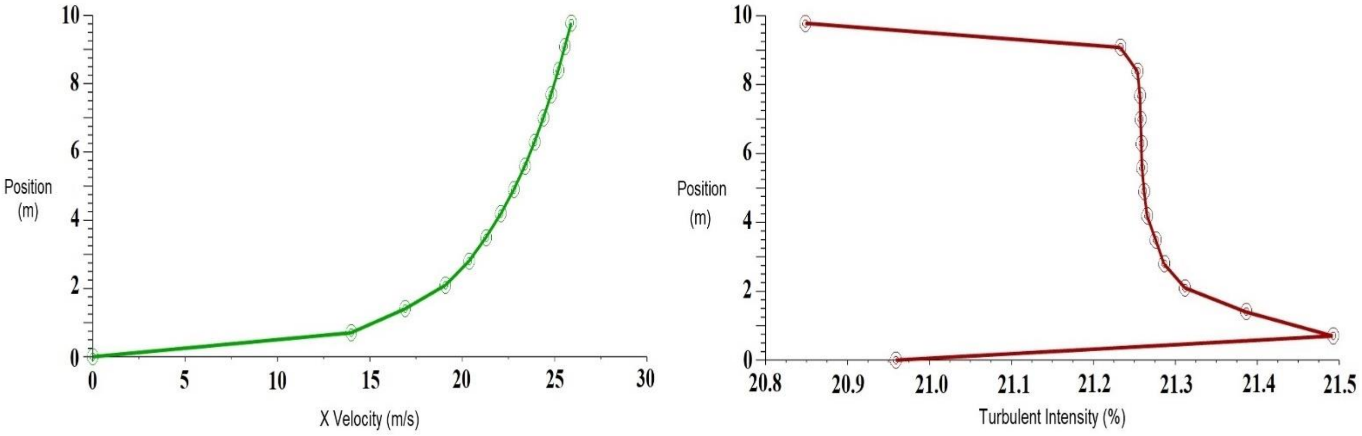

(a) Inlet velocity profile (b) Turbulence intensity profile

Figure 7. Inlet velocity and turbulence intensity profiles.

The inlet velocity and turbulence intensity profiles correspond to those analyzed in the Engineering Sciences Data Unit (ESDU) for an open terrain (ESDU, 1974). The graphs generated by the current study more closely match the wind tunnel experimental results from (Jubayer, 2014), mainly at lower heights above the ground.

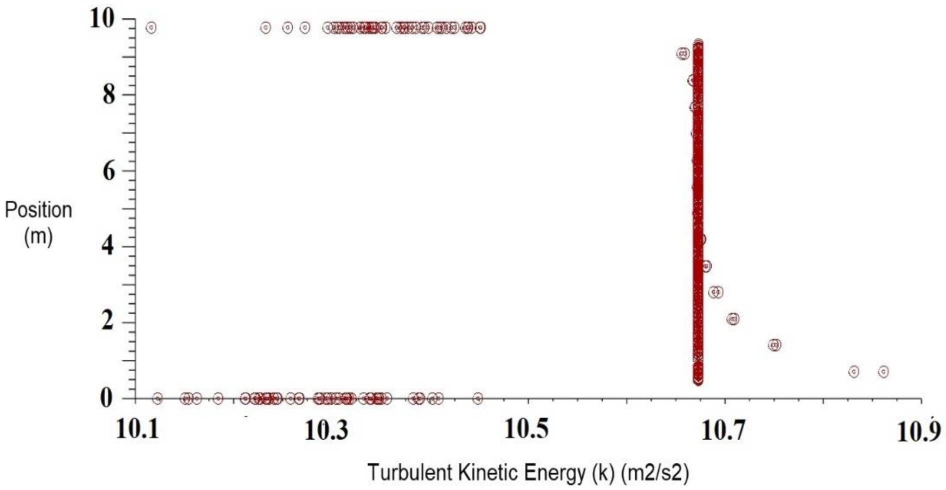

Figure 8. Turbulent kinetic energy (k) at the inlet of the computational domain.

Figure 8 illustrates the turbulence kinetic energy (k) at the inlet boundary. According to the formula (Eq. 2.2.2.3), the turbulence kinetic energy is not a function of the domain height. Therefore, the TKE values are constant at all height positions, presented as a straight line in Figure 8 (k=10.68 m²/s²). However, at 2-4 meters above the ground, the turbulence kinetic energy reaches a maximum value of 10.86 m²/s². This variation is owing to the improper discretization of the first grid point by the ANSYS software (Richards & Norris, 2011).

The boundary conditions for the current study are summarized in Table 2 :

Table 2. Boundary Conditions description.

	Description
Inlet	Logarithmic velocity profile, given by: $u^* = \frac{U_{ref}\,\kappa}{log\left(\frac{z_{ref}+z_0}{z_0}\right)}$ (Hargreaves & Wright, 2007). The open terrain roughness height of 0.03 m., the von Karman constant is 0.4, and model constant of 0.09 for k.
Outlet	Zero gradient. Gauge pressure of 0 Pa.
Sides	Symmetry Condition.
Top	Constant velocity at the top boundary based on the ABL profile assumed at the inlet.
Bottom	No-slip rough wall for open terrain exposer with a standard aerodynamic roughness height of 0.03 m, and roughness constant of 0.5.
Panel	No-slip shear condition, with a standard wall roughness option.

3.2.2 Mesh size and mesh sensitivity study

The meshing approach used is Automatic, in which all parts of the body are meshed simultaneously using the Patch Conforming Tetrahedron Mesher algorithm, with an advancing-front point insertion technique to refine the mesh (ANSYS, 2010). Different examples with coarser and finer meshes are utilized to increase the accuracy of the analysis and check the independence of the solution and the grid. Three face size meshes are performed, two by refining the panel and the area near the flow separation, while the third face size has been applied to the entire computational domain.

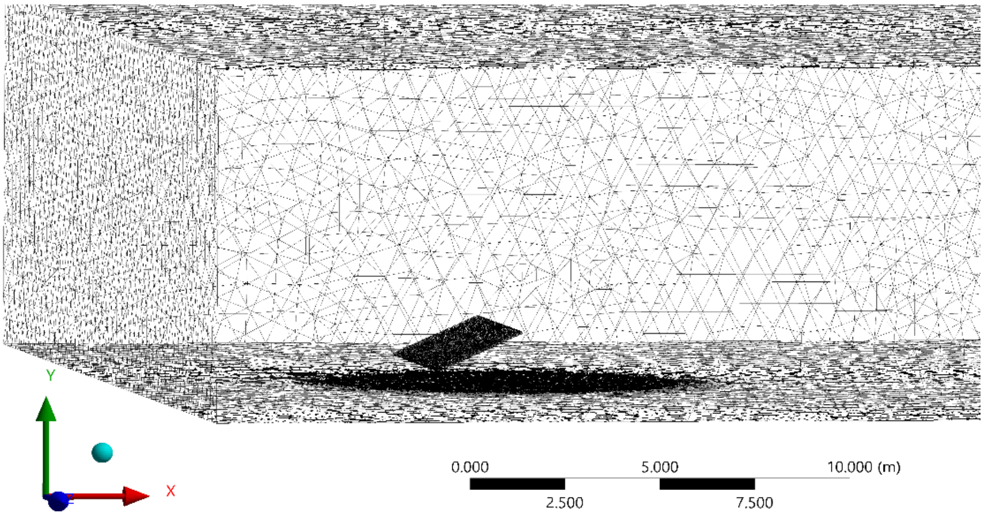

Figure 9. Mesh side view of the computational domain.

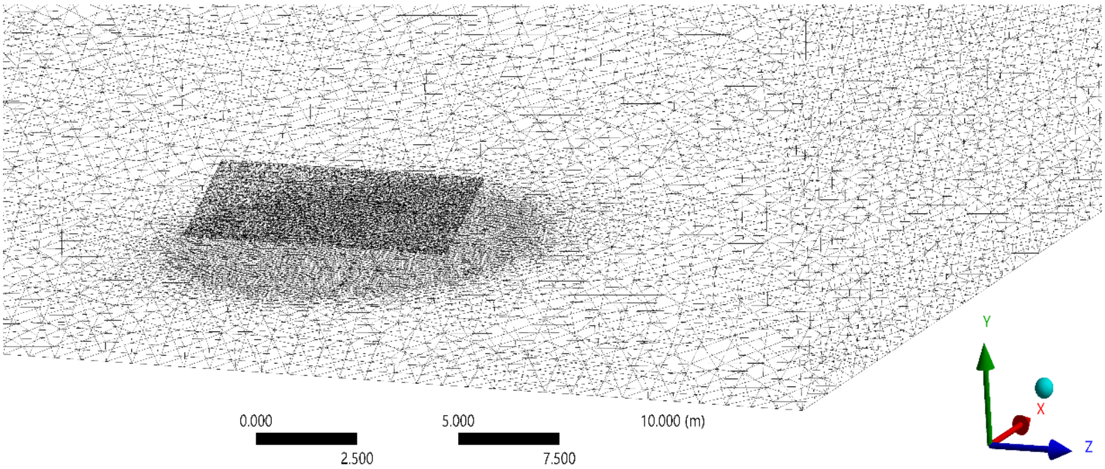

Figure 10. Mesh view of the stand-alone solar panel.

The default mesh consists of 1.66 million elements. The element's size of the computational domain was set to 0.7 m. The solar panel was refined with an element size of 0.09 m, a sphere radius of 4.5 m and an element size of 0.12 m for all topologies within the sphere field around the panel.

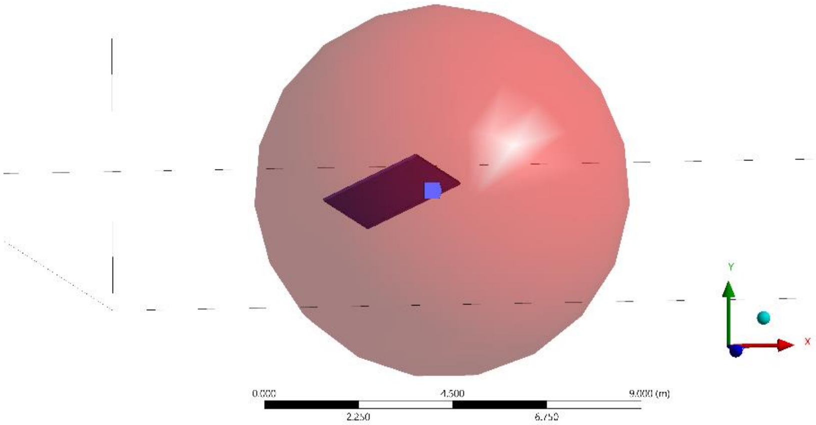

Figure 11. Sphere of influence around the panel.

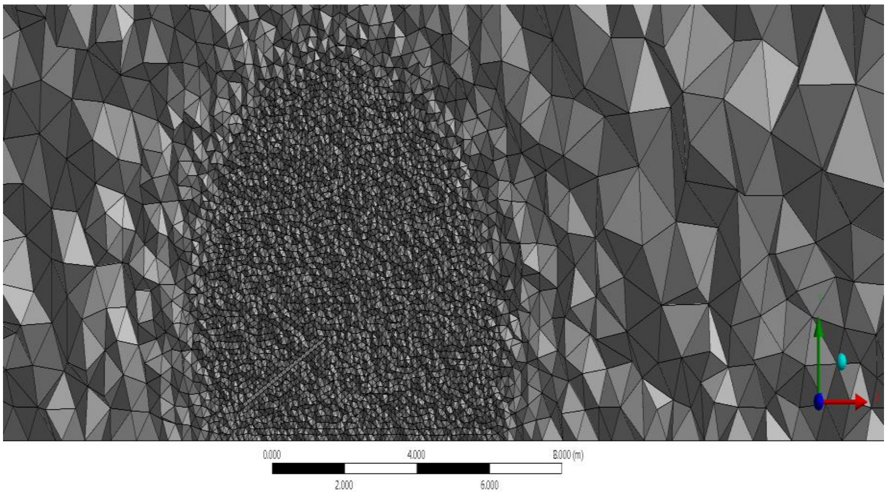

Figure 12. Mesh section plane view of the domain.

Table 3 shows the total number of cells in the grids. The grid has 1.66 million cells, which is closer to the grid employed by (Jubayer, 2014). Only the case mesh was created with a 25° tilt angle, demonstrating that further refinement of the computational domain leads to a minor improvement. These can be verified using the calculated coefficients in Figure 13.

Table 3. Drag and lift coefficients using different meshes.

	Drag Coefficient	Lift Coefficient
Mesh 1 (250473 elements)	0.9466	-1.9443
Mesh 2 (601387 elements)	0.9724	-1.9901
Mesh 3 (1663163 elements) - Default	0.9825	-1.9977
Mesh 4 (4325448 elements)	0.9823	-1.9857

The numerical simulation results in Table 3 show that the refinement of the mesh around the solar panel results in a slight variation in the drag and lift coefficients. However, at the largest grid size of 4.3 million elements, there is a slight increase in the lift coefficient, possibly related to the limited number of iterations where the simulation was stopped. Furthermore, the finer the mesh size, the more difficult and more time to achieve a stable residue. Otherwise, the third mesh was considered as a reference model in this chapter due to its affinity to the mesh used by (Jubayer, 2014).

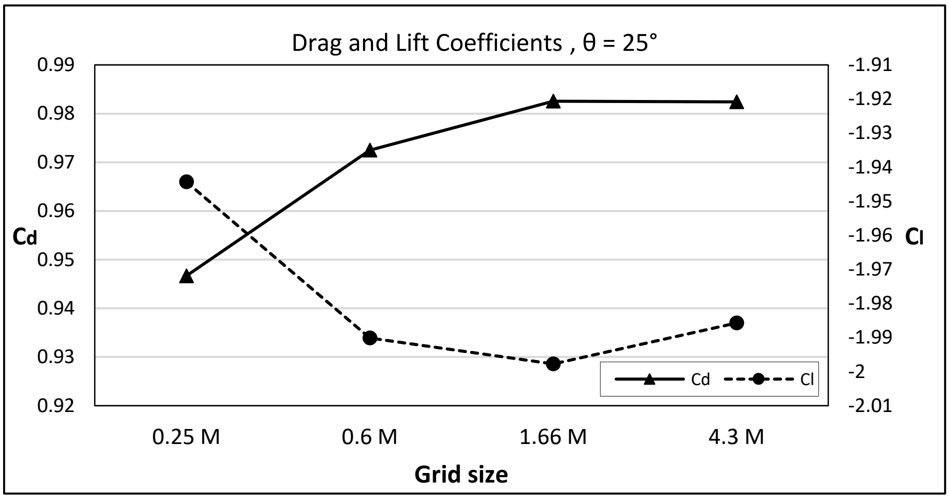

Figure 13. Drag and lift coefficients at different grid sizes.

3.3 Results and discussion

The velocity contour in the XY plane is shown in Figures 14 and 15 at different degrees of inclination and incident wind directions of 0° and 180°. The ABL function defines the inlet velocity profile in the range of 0 to 26 m/s at the entrance of the incoming flow. The velocity separation in the region closer to the back of the panel is clearly visible, particularly at the higher tilt angle of 45°. The more the panel is tilted, the more the airflow is separated.

The ground roughness reduces the air speed at the bottom zone of the domain, while the separation area increases the flow velocity in the lower area below and after the panel, as shown in Figures 14 and 15. In addition, the flow acceleration distribution was considerably noticed above the highest tilt angle.

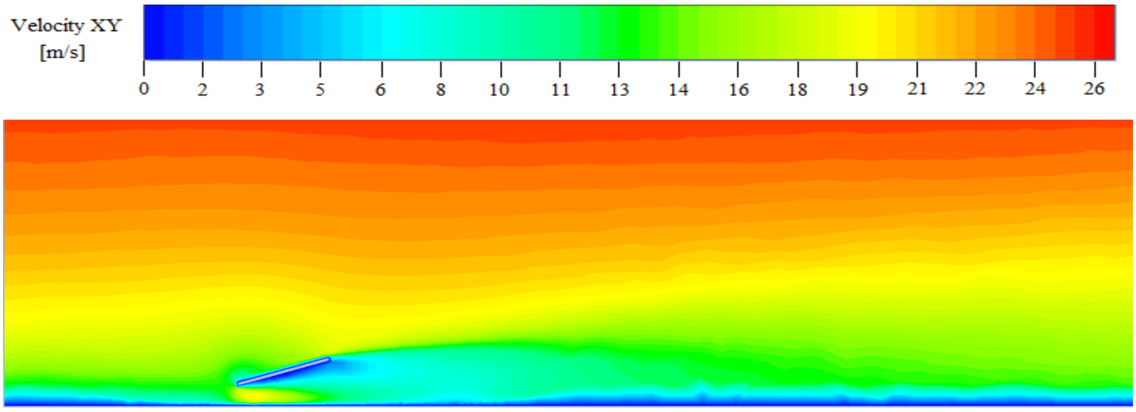

15° tilt angle – 0° wind direction.

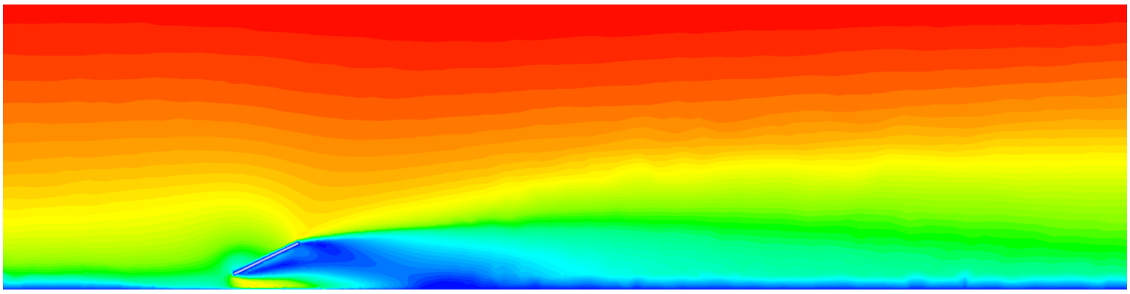

25° tilt angle – 0° wind direction.

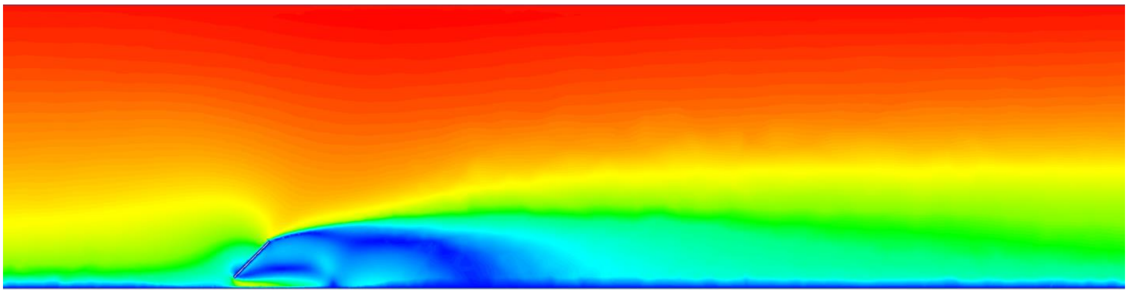

45° tilt angle – 0° wind direction.

Figure 14. Velocity contour for 0° wind direction at 15°,25°,45° tilt angles.

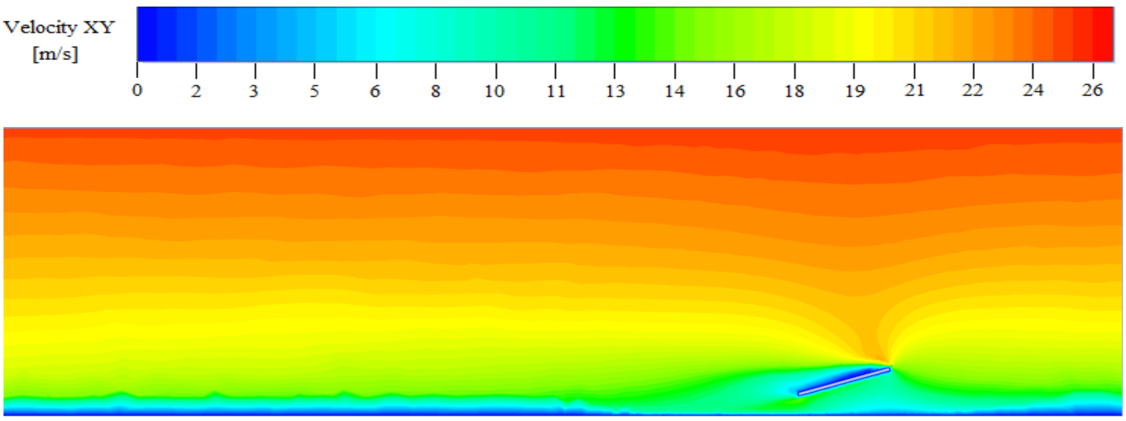

15° tilt angle – 180° wind direction.

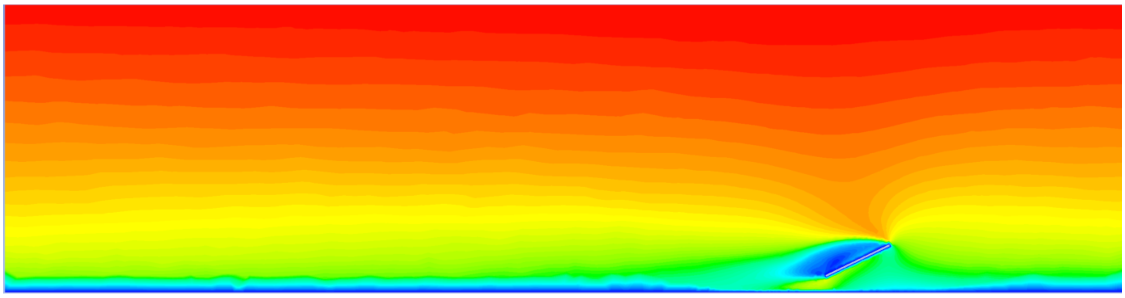

25° tilt angle – 180° wind direction.

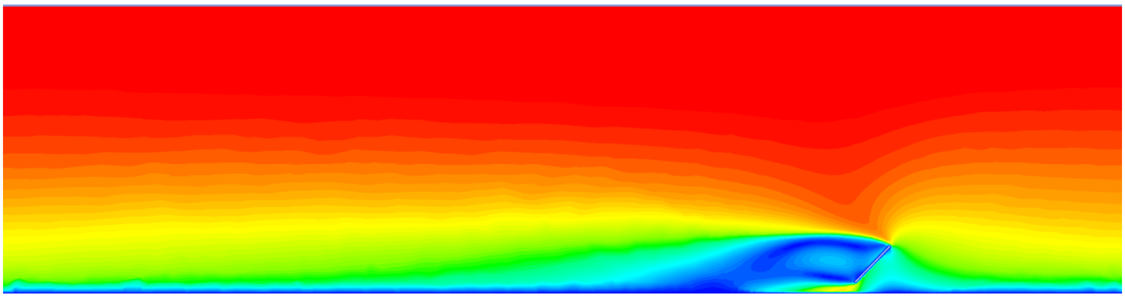

45° tilt angle – 180° wind direction.

Figure 15. Velocity contour for 180° wind direction at 15°,25°,45° tilt angles.

Figure 16 shows the velocity streamlines in different configurations. Due to the inclination of the panel, the vortex on the backside (0°,45°) and front side (135°,180°) is completely disordered. Beyond the panel, the wind speed separation decreases while increasing at the upper and down edges of the model. When the wind blows from 45° and 135° wind directions, the corner vortices are significantly larger than 0° and 180° wind directions.

The incoming flow from 0° and 180° wind directions create two parallel vortices at the bottom edges of the panel, but the recirculation streamline counters have a similar distribution and shape, while the vortices rotate differently from side to side of the stand-alone PV. However, a single vortex can be seen in 45° and 135° wind directions.

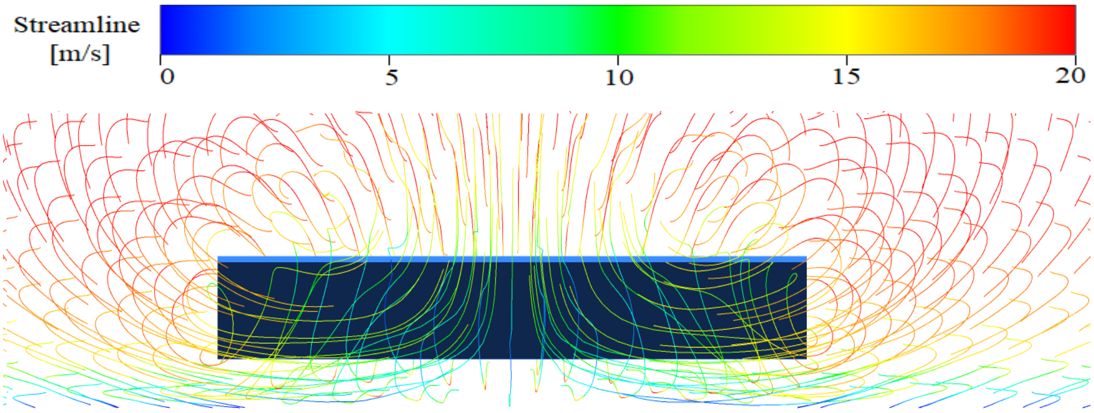

25° tilt angle – 0° wind direction – Back side

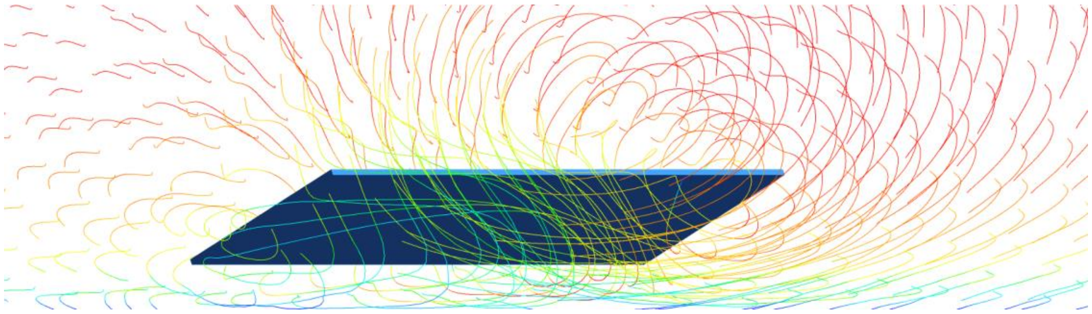

25° tilt angle – 45° wind direction – Back side

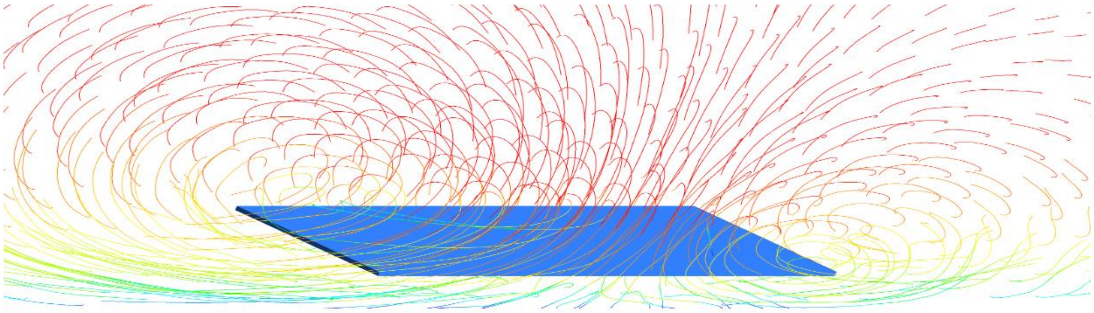

25° tilt angle – 135° wind direction – Front side

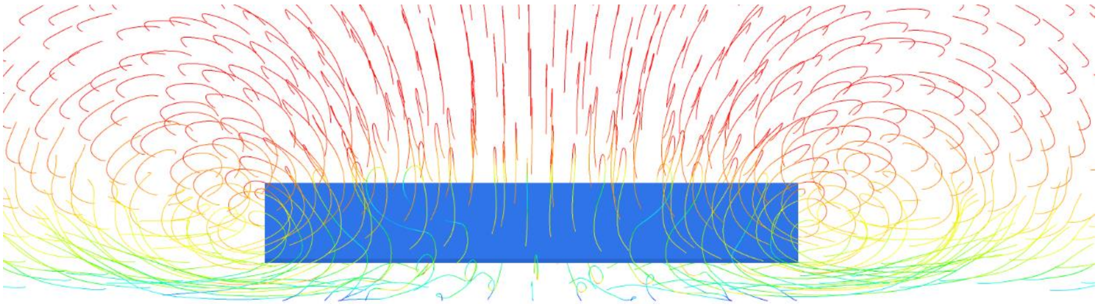

25° tilt angle – 180° wind direction – Front side

Figure 16. Velocity streamline at different wind directions (back and front sides).

3.3.1 Drag and lift coefficients

ANSYS Fluent is used to estimate the drag and lift coefficients for different panel inclinations and wind directions, and the findings are compared to those researched by Jubayer, C. M. Only the air flow type is considered as a steady-state from the beginning of the simulation, while Jubayer's simulation reached the steady-state after 5 s flow time based on the pressure around the panel (Jubayer, 2014). With the exception of flow conditions, all other parameters including domain, boundary conditions, mesh size, and reference values were configured similarly to the Jubayer research.

The reference values are based on the wind velocity at the lower part of the panel, which results in a Reynolds number of 2.13×10^6.

Table 4. Reference Values.

	Reference Values
Area (m^2)	17.856
Density (kg/m^3)	1.225
Length (m)	2.48
Velocity (m/s)	12.5458
Temperature (K)	288.16
Viscosity (kg/m. s)	1.7894×10^{-5}

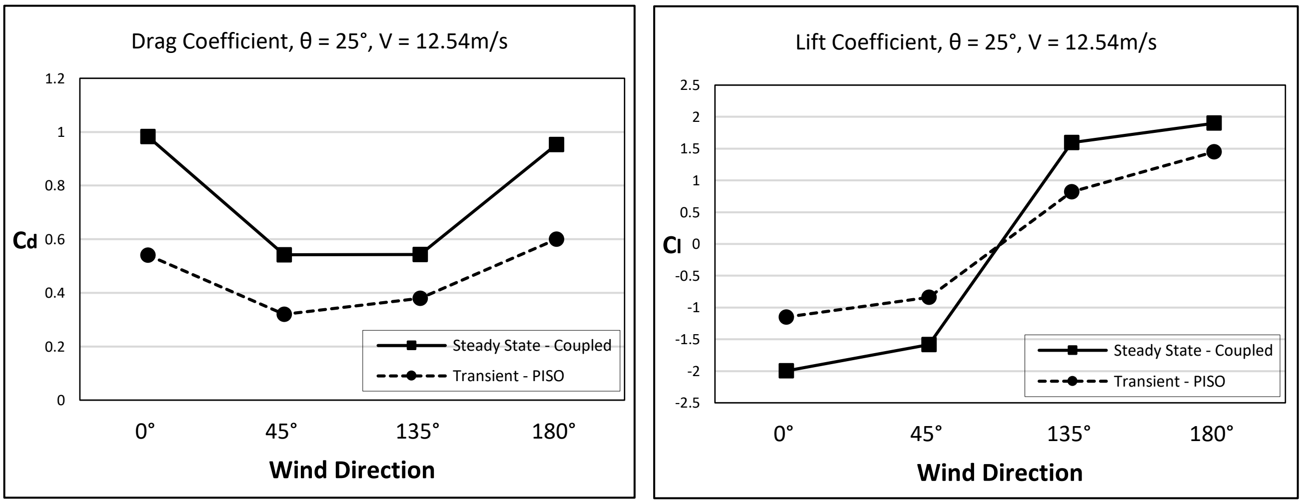

Figure 17. Steady state and transient drag and lift coefficients at 25° tilt angle.

Table 5. Drag and lift coefficients at 25° tilt angle comparison with (Jubayer, 2014).

Wind Direction	Current study – Steady state		Jubayer, C. M. - Transient	
	Drag Coefficient	Lift Coefficient	Drag Coefficient	Lift Coefficient
0°	0.982	-1.997	0.54	-1.15
45°	0.542	-1.584	0.32	-0.84
135°	0.543	1.593	0.38	0.82
180°	0.952	1.899	0.6	1.45

The results of this study, as well as those of (Jubayer, 2014), are shown in Table 5. Instead of a transient and PISO solver, a steady time with coupled solver was used with the same reference values, computational domain, and mesh sizes in both studies. Figure 17 reveals that the shape of the curve is in a reasonable orientation. On the other hand, the steady-state simulations lead to slightly higher results due to the use of different software, flow types and solvers, which are considered suitable for the current status. The comparison demonstrates that the coefficients at 0° and 180° wind directions are higher than at 45° and 135° wind directions, with the most significant mean values at 180° wind direction, where the wind flow reaches the panel from its lower surface.

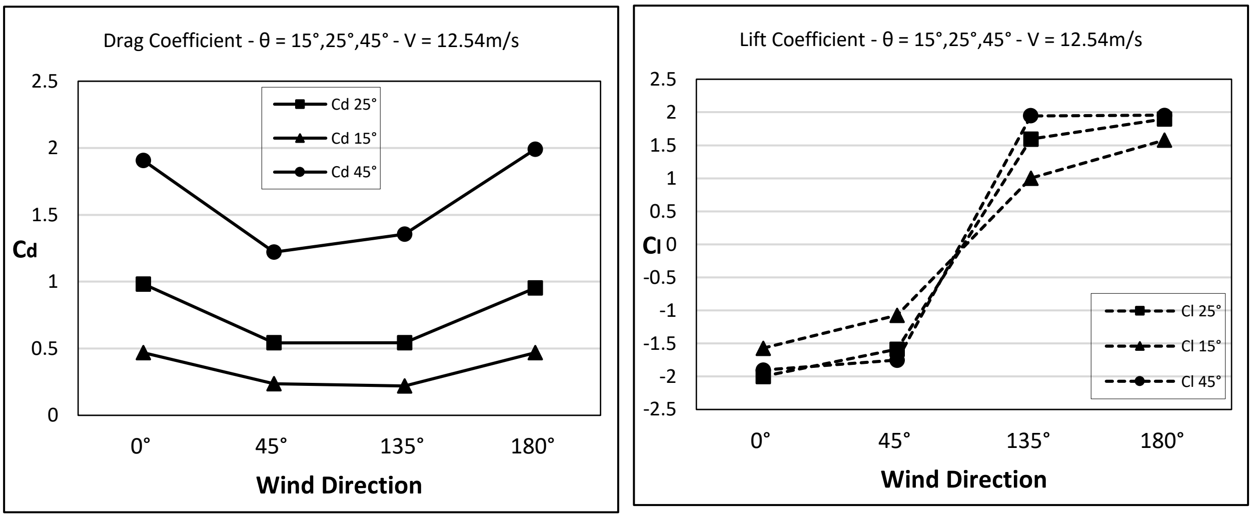

Figure 18. Drag and lift coefficients at different tilt angles and wind directions.

Figure 18 illustrates the variation of drag and lift coefficients for different wind directions and panel inclinations. The findings are obtained using the steady-state flow and coupled solver. The Reynolds number of 2.13x10^{6}, which refers to the velocity of 12.5458 m/s at the height of the lower edge of the panel, remains constant in all cases. The drag and lift curves continued to increase as the tilt angle increased, which is acceptable due to the high pressure on the upper than the lower surface of the panel where the flow operates. As a result, a larger angle of inclination is undesirable for a stand-alone ground mounted panel installation to avoid intensive forces acting on the panel. In addition, unlike the rest of the configurations, there is a slight variation in the coefficients when the wind changes direction at the lowest tilt angle of 15°.

3.3.2 Pressure Coefficient

This section describes the distribution of panel pressure on the top and lower surfaces for different wind directions. Throughout the solar panel, the pressure coefficients ranged from -254.9 [Pa] to 151.3 [Pa]. The leading surface exposed to the incoming wind has a higher pressure. The pressure on the leading edge of the top surface of the panel increases slightly as the panel angle increases when the wind angle is set to 0°.

Negative pressure coefficients are observed on the lower surfaces due to flow separation behind the panel, as shown in Figure 19. The wake pressure rises in the opposite region of the highest points at the windward surface.

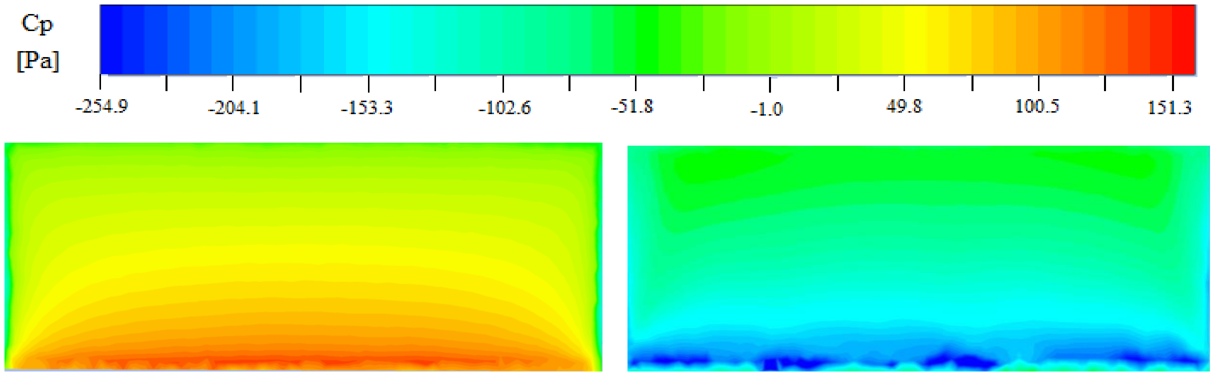

Upper Surface Lower Surface

15° tilt angle – 0° wind direction

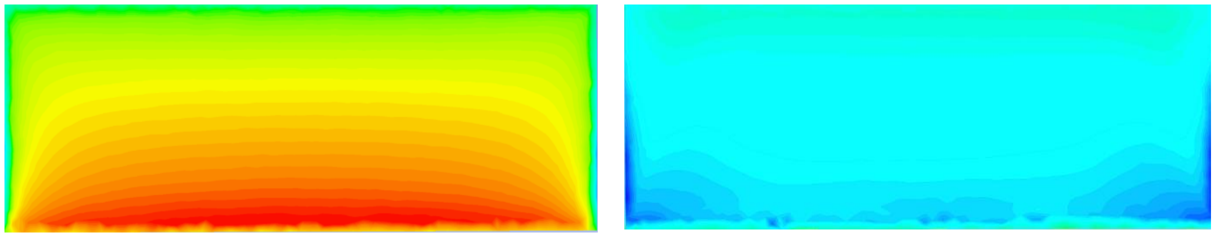

Upper Surface Lower Surface

25° tilt angle – 0° wind direction

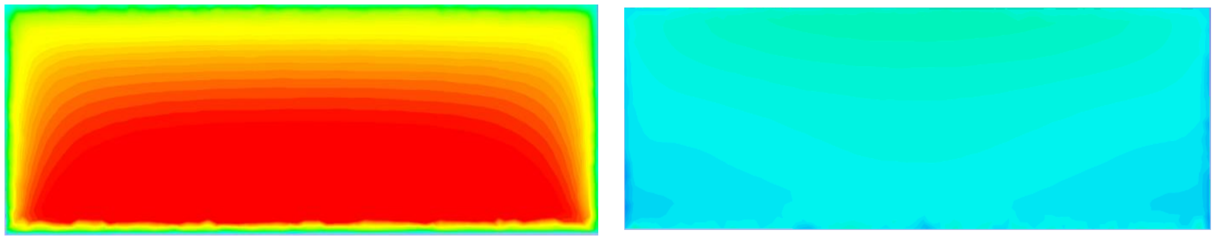

Upper Surface Lower Surface

45° tilt angle – 0° wind direction

Figure 19. Pressure coefficient at the upper and lower surfaces for 0° wind direction.

The mean pressure contours in Figure 20 show that the coefficients at the incoming wind of 0° and 180° are almost similar in terms of pressure distribution, while the pressure distribution is reversed from the down edge to the top one. Otherwise, changing the wind angle switches the upper and lower values for the surface. The same behavior can be seen in 45° and 135° wind directions, however, the mean pressure distribution for each surface gradually rises from the corner edges.

At the extreme limits of the panels, negative pressures can be observed in all cases, which is more important for an approaching wind of 45° and 135°, where the mean pressure fluctuates in a range of -26.4 and -254.9 [Pa].

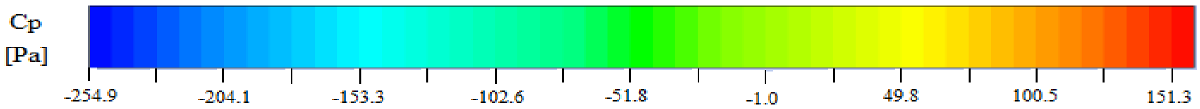

25° tilt angle – 0° wind direction

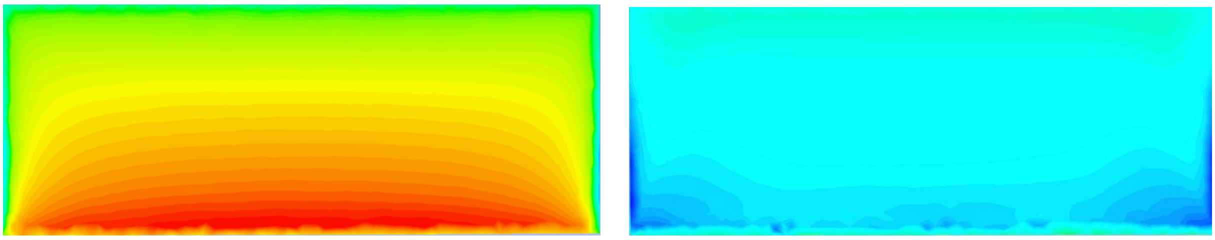

Upper Surface Lower Surface

25° tilt angle – 45° wind direction

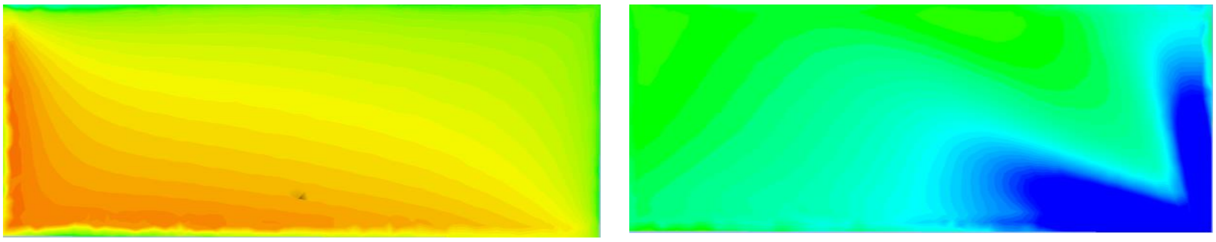

Upper Surface Lower Surface

25° tilt angle – 135° wind direction

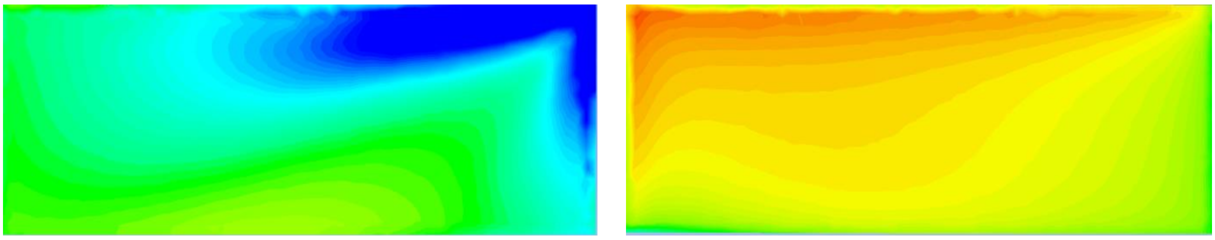

Upper Surface Lower Surface

25° tilt angle – 180° wind direction

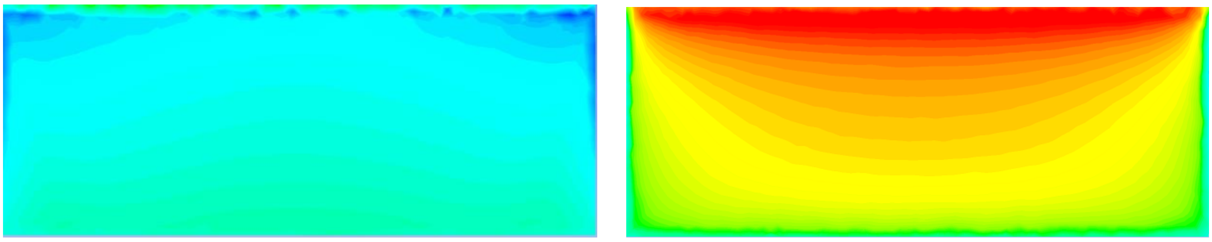

Upper Surface Lower Surface

Figure 20. Pressure coefficient at the upper and lower surfaces for different wind directions.

3.4 Summary

Using the Reynolds-Averaged Navier-Stokes (RANS) method, the workflow for this chapter has been divided into four parts: mesh sensitivity analysis, streamline and velocity contours, drag and lift coefficient studies, and pressure distribution.

The numerical simulation results show that both steady state and transient simulations show a good agreement on aerodynamic loads. This correlation is related to the flow stability after 5 seconds in the transient simulation. Otherwise, increasing the angle of inclination causes a significant increase in the drag and lift coefficients over the panel. At 180° and 0° wind directions, respectively, the largest positive and negative lifts can be seen. The positive pressure increases vertically from the leading edges for 0° and 180° and diagonally from the corners of the panel for 45° and 135° on most windward surfaces. For 0° and 180° wind directions, the streamline vortex counters are more separated and symmetrical than 45° and 135°.

When the solar panel is tilted, all of the mentioned factors and characteristics increase, notably the aerodynamic loads. To avoid larger stresses on the panels, an inclination angle of more than 45° is not recommended.

Chapter. 4

IV. Wind load analysis of two separated solar panels

4.1 Dimensions of the domain

The dimensions of the computational domain provided in this section are identical to those of the previous chapter. Based on the specific recommendations of the COST guidelines, the overall domain size is 21.4H x 6H x 24.2H, where the domain dimensions are calculated from the object height H (Franke et al., 2011). Meanwhile, a separate stand-alone solar panel has been established to investigate the effect of the distance between two separate panels on the drag and lift coefficients around the panels. Four gap distances are examined, the first model refers to a single panel of double width (2xW), the total dimension of the panel becomes 2.48m (B) x 14.4 m (W) which corresponds to a distance of 0 m. The other three cases are 0.5m, 1.5m, and 3.5m.

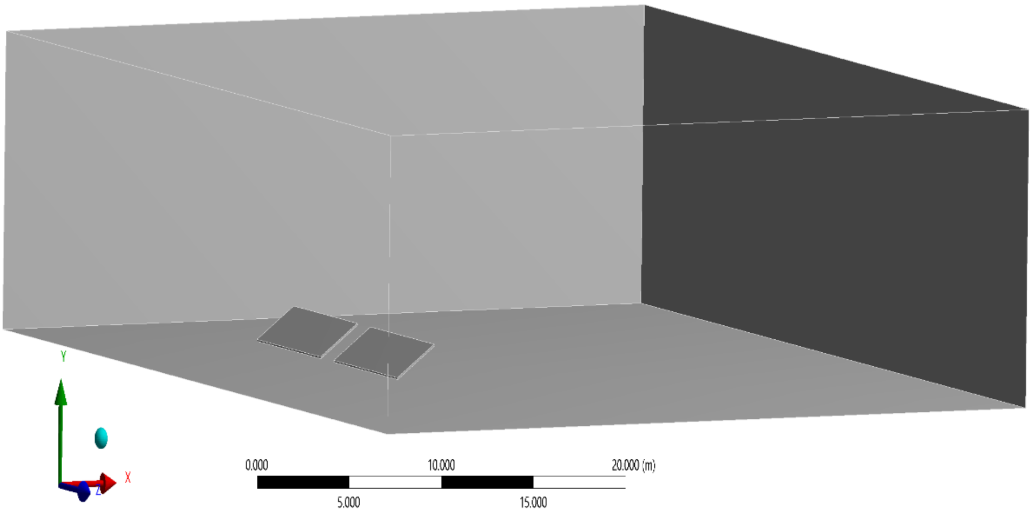

Figure 21. Computational domain of two separated panels.

These panels are placed at an angle of inclination of 25°, with the wind direction computed from 0° and 180°. The three-dimensional computational domain and panels are shown in Figure 21.

4.2 Computational setup

The patch conforming tetrahedron approach is employed, the mesh consists of 1.884 million elements. The element's size of the computational domain was set to 0.7 m. The solar panels are refined with an element size of 0.1 m. The number of cells around the panels was increased using the sphere of influence option, setting the sphere radius to 8.5 m, and the element size of all volumes within the sphere field to 0.2m. The 3D mesh view of the computational domain is shown in Figure 22.

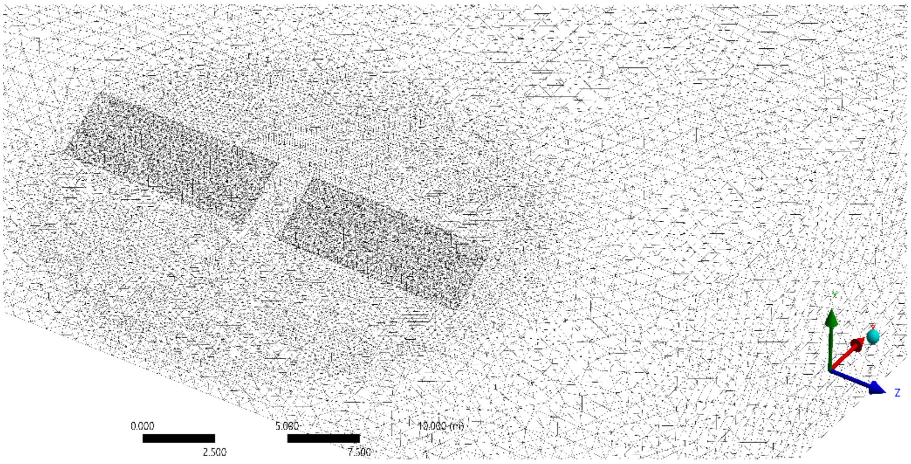

Figure 22. Mesh view of the computational domain and the panels.

Figure 23 shows a two-dimensional ZY section plane view with the panels represented by thin lines representing their thickness. The mesh is more focused around the panels so as to reduce the number of cells in the computational domain.

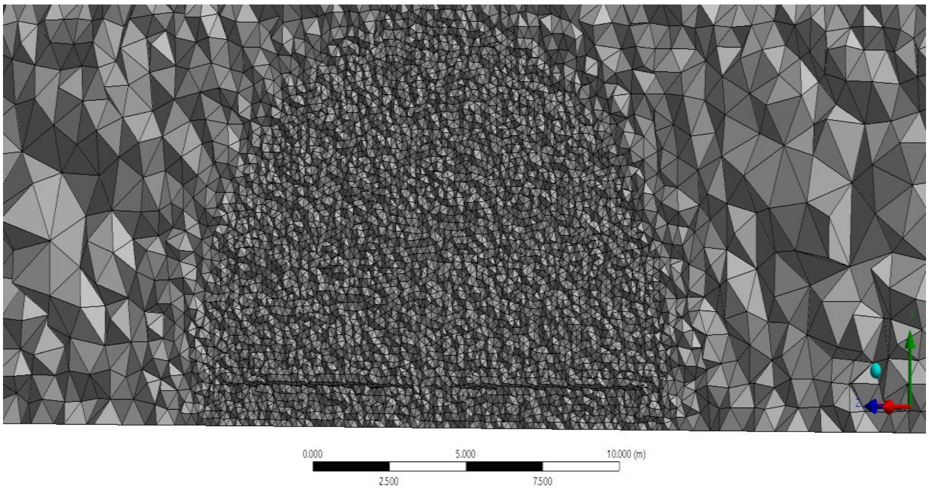

Figure 23. Section plane ZY view of the mesh.

4.2.1 Boundary conditions

The inlet and top surface boundary conditions are defined by the imported User-Defined Function (UDF) (see appendix). The UDF is split into three parts: velocity, turbulent kinetic energy, and turbulent dissipation rate profiles. We have assumed a wind speed of 26 m/s at an altitude of 10 m in the inlet region. Here, the upper limit is a constant velocity of 26m/s along with the computational domain. The panel and lower boundary zones are considered to be a no-slip shear condition with a roughness constant of 0.5 and a roughness height of 0 and 0.03 m, respectively. In the outlet zone of the computational domain, the gauge pressure was assumed to be zero pascal. A detailed description of the boundary conditions is given in Table 2.

4.3 Results and discussion

The results shown in Figure 24 confirm that the space between two separate panels has a significant impact on flow circulation. The velocity streamline behavior of the first model is identical to that of the previous chapter, where two parallel vortices are formed behind the side edges of the panel. At a distance of 0.5 m, the incoming wind flow passes through the gap and creates higher velocity turbulence that produces more pressure than the first model. As the gap grows, more wind enters the opening, which increases the velocity and disorder the flow in that area.

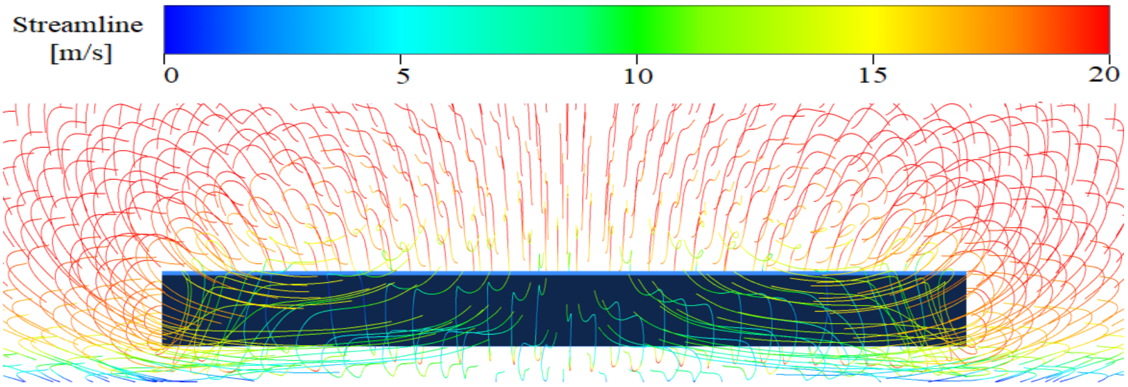

No Gap – 0° wind direction – Back Side

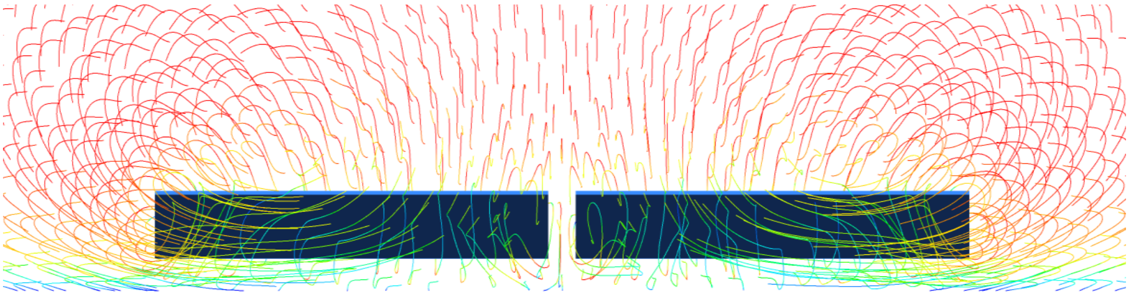

0.5 m Gap – 0° wind direction – Back Side

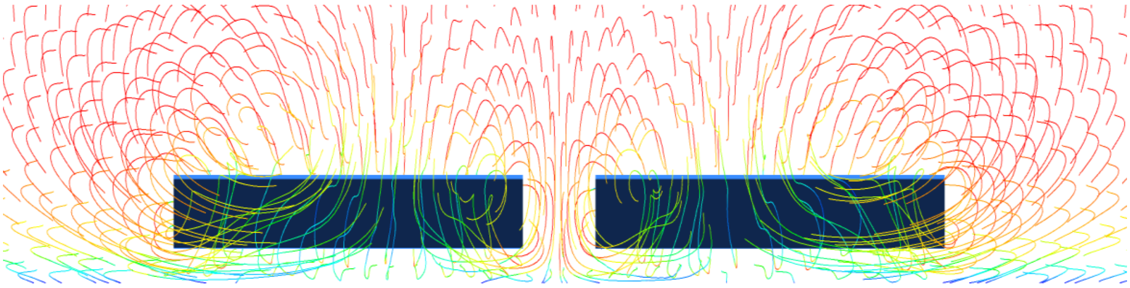

1.5 m Gap – 0° wind direction – Back Side

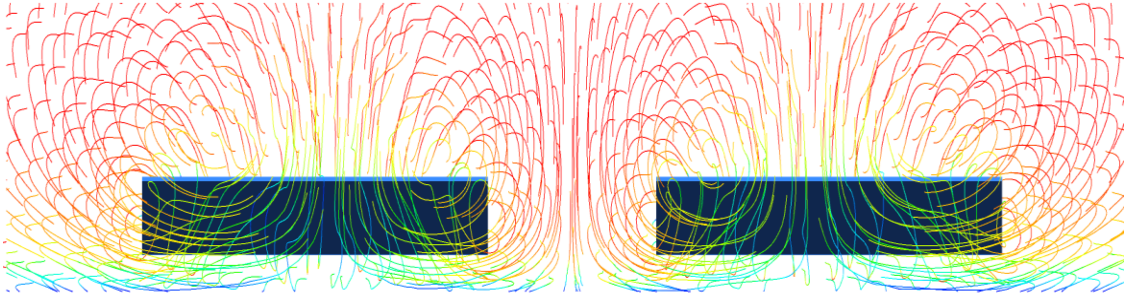

3.5 m Gap – 0° wind direction – Back Side

Figure 24. Velocity streamline at different gap distances between two panels.

4.3.1 Drag and lift coefficients

A comparison of drag and lift at different gap distances are illustrated in Figures 25 and 26, where the zero meter spacing provides twice the width of the single panel previously examined in the first chapter. The same reference values were employed, resulting in a Reynolds number of 2.13x10^6. Undoubtedly, the trends shown in Figures 25 and 26 demonstrate that as separation increases, drag and lift tend to converge slightly to the single panel values. However, according to the findings, the distance must be more than 3.5 meters to avoid significant stresses on the side edges of the panel.

The movement of the coefficient graphs at a wind direction of 180° agrees well with the simulation performed a wind angle of 0°. The short separation distance results in more wake behind the panels, so increasing drag and lift to twice that of a single PV panel.

Figure 27 shows the coefficients of the first and second panels. As the gap distance increases, the drag coefficient drops significantly. However, the lift coefficient corresponding to the same wind direction changes slightly as the distance increases. Furthermore, Figure 27 demonstrates that there are no considerable variations in the coefficient values between the two panels.

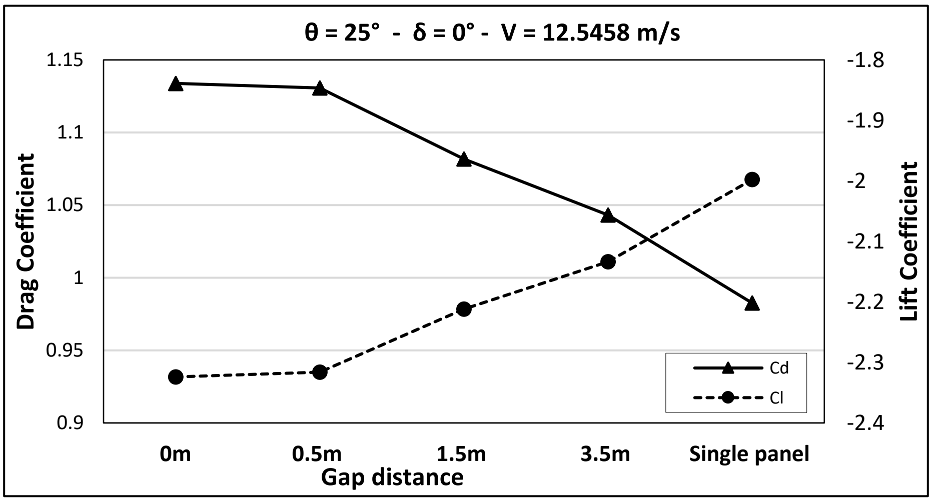

Figure 25. Drag and lift coefficients for different gap distances at 25° tilt angle and 0° wind direction.

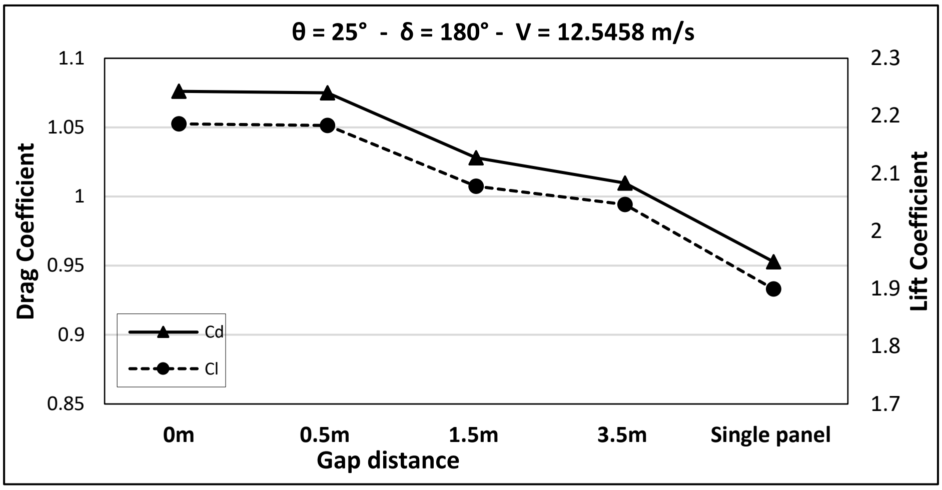

Figure 26. Drag and lift coefficients for different gap distances at 25° tilt angle and 180° wind direction.

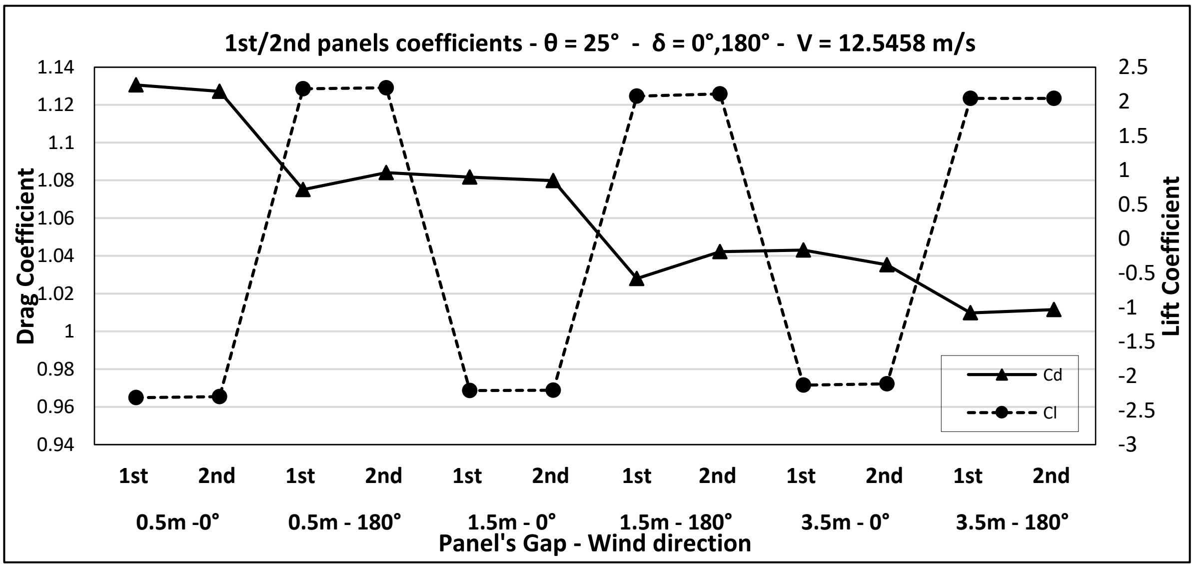

Figure 27. First and Second panels' coefficients at 25° tilt angle with 0° and 180° incoming wind.

4.3.2 Pressure coefficient

In Figure 28. The wind loads have a greater pressure gradient on the side edges closest to the separation gap than on the opposite sides. The mean pressure coefficients on the upper surfaces are symmetrical, and both panels behave in the same manner by increasing the gap distance. The highest pressure distribution is seen near the lower edge of the panels, which corresponds with the single panel analysis experienced at 0° wind direction. When considering the results of the drag and lift coefficients described in Figure 27, the different distributions at the side edges are noticeable.

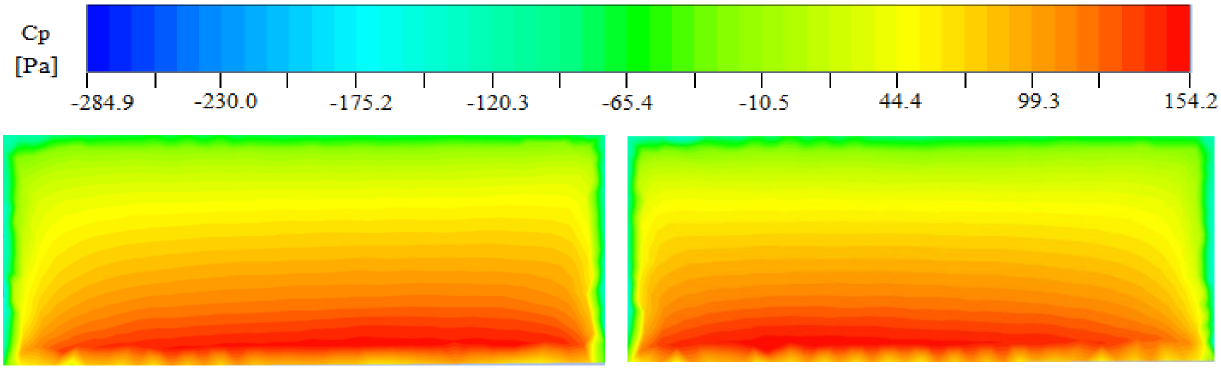

1st Panel 2nd Panel

0.5m Gap – 0° wind direction – Upper Surface

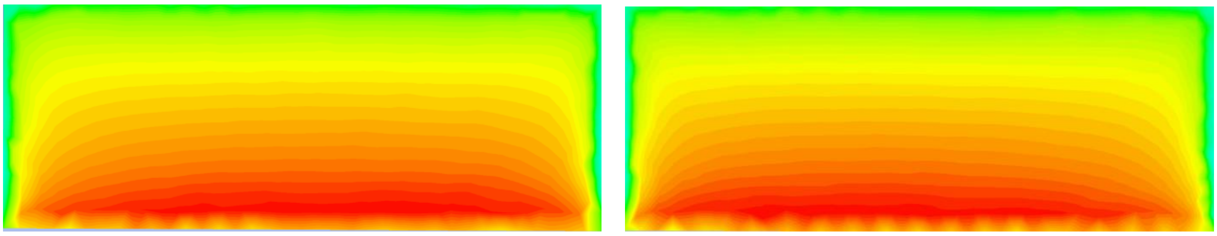

1st Panel 2nd Panel

1.5m Gap – 0° wind direction – Upper Surface

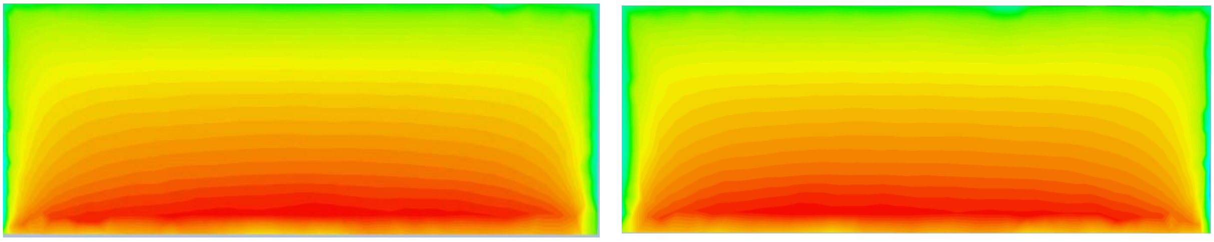

1st Panel 2nd Panel

3.5m Gap – 0° wind direction – Upper Surface

Figure 28. Pressure distribution of the first and second panels at different gap distances.

4.4 Summary

This chapter examined the effect of space distance on two separated panels. The 0-meter, 0.5-meter, 1.5-meter and 3.5-meter variants are examined. In terms of streamline separations, drag and lift, and pressure distribution, all these cases are compared to the single panel discussed in the previous chapter.

Compared to other distances, the highest pressure was observed along the side edges closest to the opening for a 0.5-meter gap, where significant wind speed was identified. Furthermore, a small gap causes more wake on the backside of the panels, creating significant pressure on the closest edges. When the spacing is larger, the aerodynamic loads decrease and the panel behaves as a single panel when the spacing is more than 3.5- meters. Therefore, it is recommended to separate the rows of solar panels as much as possible to minimize large loads, especially in diagonal wind directions of 45° and 135°.

Chapter. 5

V. Investigation over array of ground mounted solar panel

This chapter presents an investigation of drag, lift, and pressure coefficients applied on consecutive solar panels, with the number of arrays fixed in terms of size and tilt angle to 5 identical rows. The wind flow is simulated from an angle of 0°,45°,135° and 180°, and the inclination of the panel is varied to 15°,25°, and 45°.

5.1 Dimensions of the domain

As previously mentioned, the computational domain was chosen according to the COST specific standards guidelines. The panel height noted H, is used to determine the domain dimensions (Franke et al., 2011). Each array measures 2.47 m (B) x 21.9 m (W), and has a thickness of 0.07 m as shown in Figure 5. Jubayer used the same domain, setting the overall domain size to 30.2H (X) x 6.0H (Y) x 48.4H (Z) at 0° and 180° wind directions, and the computational domain increased to 36.3H (X) x 6.0H (Y) x 52.0H (Z) for 45° and 135° wind directions (Jubayer, 2014), taking into consideration the standards of the COST guidelines. Furthermore, the horizontal distance between two arrays is given as 1.04 H (Jubayer, 2014), and it depends on the panel height, which varies depending on the tilt angle. The three-dimensional view of the computational domain used in this chapter is shown in Figure 29.

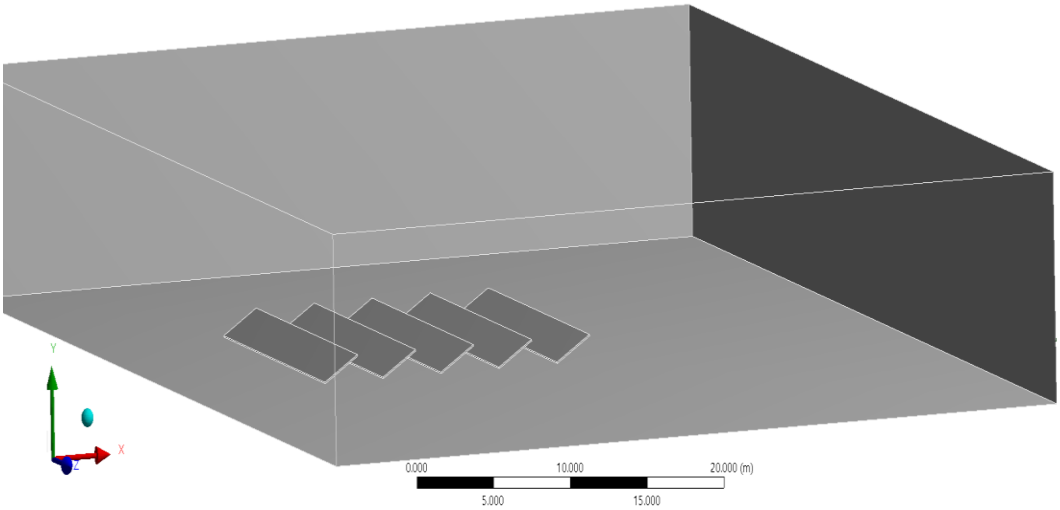

Figure 29. Three-dimensional view of the computational domain at 25° tilt angle.

5.2 Computational setup

The mesh is created using a patch conforming tetrahedron method. The average number of cells was 3.8 million elements for 0° and 180° wind directions and 4.01 million for 45° and 135°. The element size of the six faces of the domains was set to 0.7 m. Solar panels are refined with an element size of 0.1 m. The area near the consecutive array is refined using a sphere of influence with a radius of 8.5 meters, and an element size of 0.2 meters for all regions within the sphere field. However, the meshes constructed by Jubayer have a total cells of 2.2 million and 2.1 million (Jubayer, 2014). These variations in cell number are related to the hybrid approach used by Jubayer, which combines prismatic, hexahedral, and tetrahedral types (Jubayer, 2014).

In addition, an atmospheric boundary layer profile with a wind speed of 26 m/s at a heigh of 10 m was chosen at the inlet boundary. No-slip smooth and rough walls are respectively used for the panels and bottom face. At the outlet, there is a zero gauge pressure, and the top face of the domain has a constant velocity value. Figure 4 shows the velocity profile and turbulence intensity plots. The side and XY section views of the global computational domain are shown in the following Figures (Figure 30 and Figure 31).

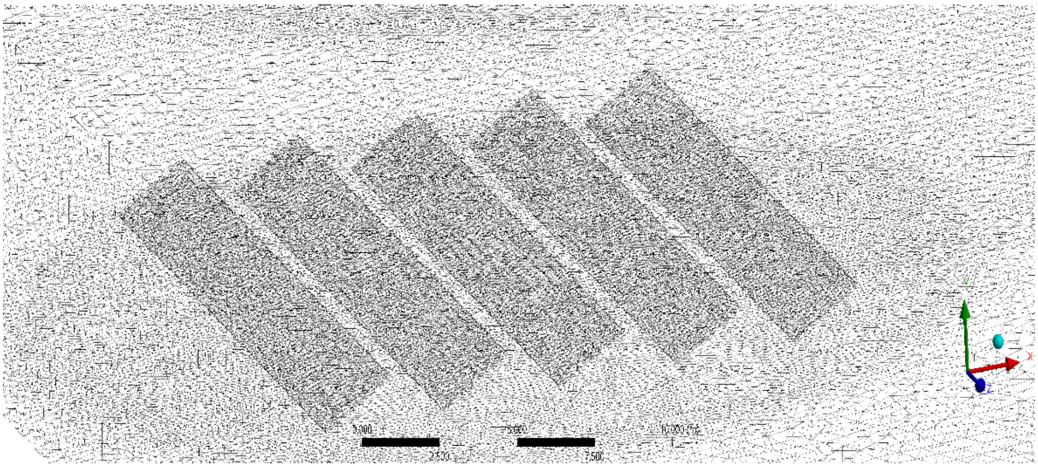

Figure 30. Mesh view of the consecutive array.

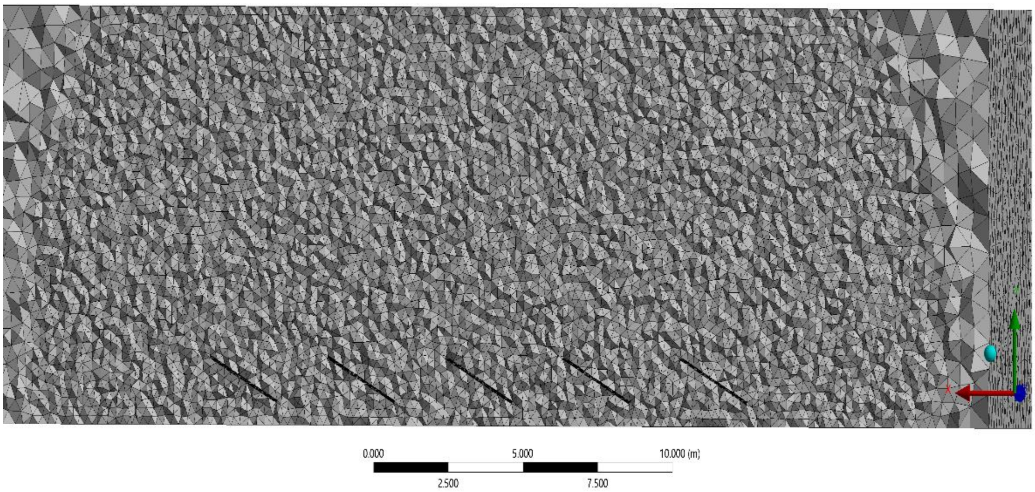

Figure 31. XY section plane of the computational domain mesh.

5.2.1 Boundary conditions

Table 2 shows the boundary conditions of the domain. The inlet and upper boundaries are defined by the UDF functions described in the appendix section. The outlet boundary pressure is set to zero pascal gauge. At the lower boundary, a standard roughness model with a roughness height of 0.03 m is applied. The walls on the side faces of the domain are assumed to be symmetrical. A detailed description can be found in section 3.2.1.

5.3 Results and discussion

ANSYS Fluent simulation was run on several models to assimilate fluid flow around five consecutive arrays. The velocity contours for 25° tilt angle and 0°,180° wind directions are shown in Figure 32. The separation zone increases from row to row, and the wind velocity reaches zero velocity after the last array, especially with 0° incoming flow.

Concerning flow separation, the first row behaves similarly to a single panel presented in the first chapter, with the flow acceleration increasing towards the upper and lower edges. While in the rest arrays, where the panels are exposed to low incoming wind speed, the wind separation becomes more significant. The ABL profile can also be observed at the domain inlet where the wind speed varies from 0 m/s at the ground due to roughness, to 26 m/s at the top wall due to the constant velocity involved in the boundary condition section.

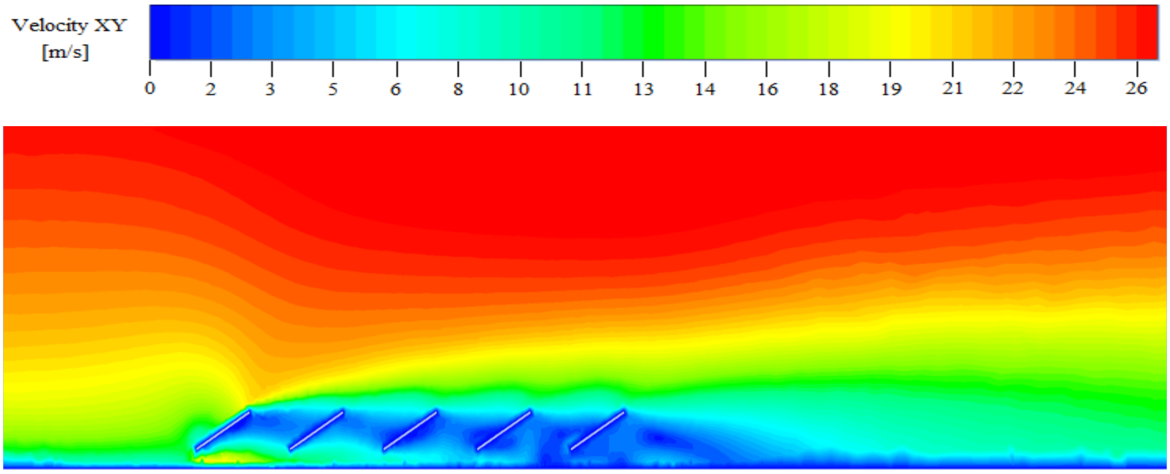

25° tilt angle – 0° wind direction

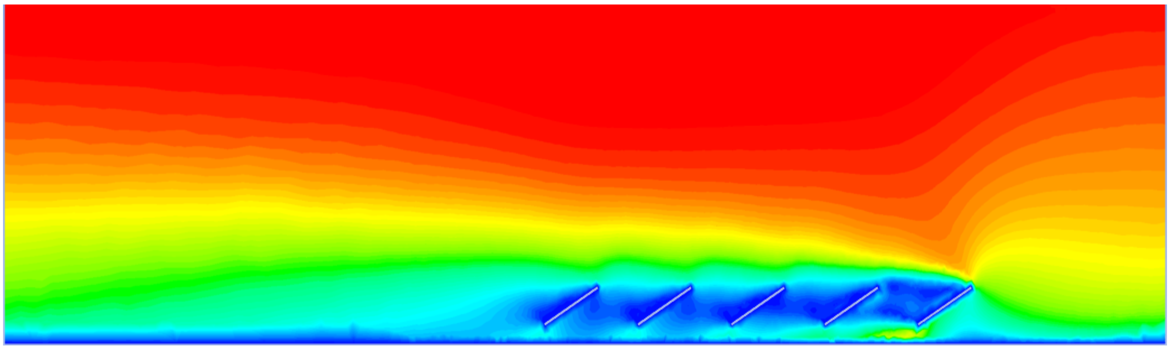

25° tilt angle – 180° wind direction

Figure 32. Velocity contours of five consecutive arrays for 25° tilt angle and 0°,180° wind directions.

5.3.1 Drag and lift coefficients

The wind flow is considered to be steady. Table 6 shows the reference values for the Reynolds number, which was estimated to be 2.96x10^6. Jubayer used the same configuration, however, the flow reached its steady state after 5 s flow time (Jubayer, 2014). The reference area represents the area of the first panel 21.92 (m) x 2.48 (m), otherwise, the other values refer to the air parameters.

Table 6. Reference Values.

	Reference Values
Area (m^2)	54.1424
Density (kg/m^3)	1.225
Length (m)	2.47
Velocity (m/s)	17.75
Temperature (K)	288.16
Viscosity (kg/m. s)	1.7894x10^{-5}

Two different analyses are discussed in this section. First, the steady state coupled solver simulations realized in this study are compared to the transient flow time reported by (Jubayer, 2014) using the PISO solver at an inclination angle of 25° (see Figure 33). Subsequently, drag and lift coefficients are calculated for different degrees of inclination and wind directions (see Figure 34).

Figure 32 shows how drag and lift coefficients behave from wind directions of 0°,45°,135°, and 180° at a tilt angle of 25°. The executed steady state simulations were compared to the transient flow, which Jubayer had previously verified. In terms of the line shape, the statistics show a great match, especially for drag acting at 45° and 135° wind directions. The most critical coefficients are observed in the first row and gradually decrease in the next arrays. These results confirm that the wake flow affects all arrays after the 1st row. The smaller coefficients are noticed in the 2nd, 3rd, and 4th rows at 0° and 180° wind directions and slightly higher in the last row. The wind load applied from the 2nd to 5th row is higher at 45° and 135° wind directions than at 0° and 180° wind direction, which can be explained by the diagonal wind, which minimizes the wake and separations between the consecutive panels.

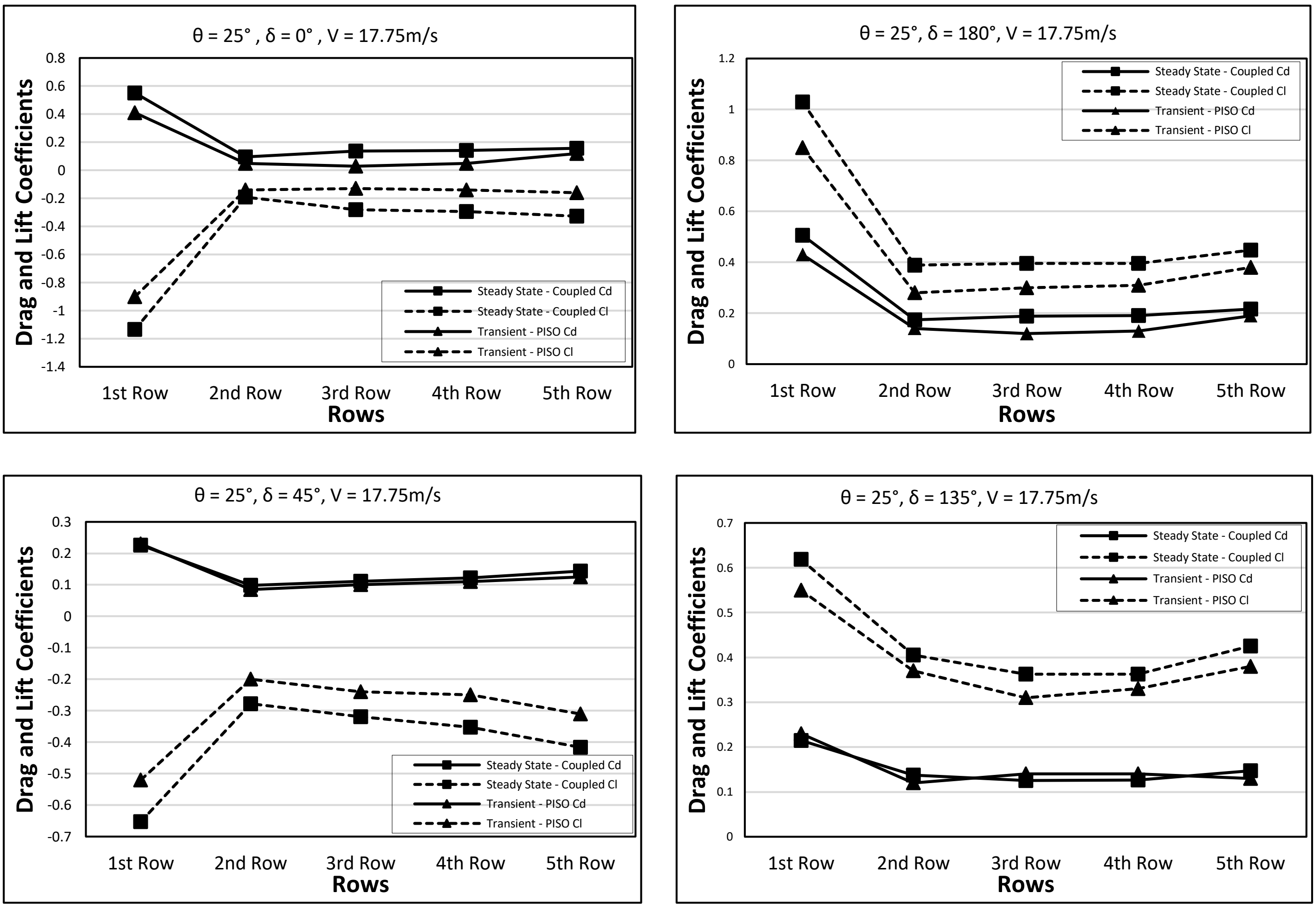

Figure 33. Drag and lift coefficients from different wind direction at 25° tilt angle.

In Figure 33, the drag and lift coefficients are simulated at tilt angles of 15°, 25°, 45°, and 0°,180° wind directions. In the first row, a significant load is observed in the first row, which becomes more crucial with an increase in the angle of inclination, while the 2nd row has minimal load due to the first row. The value varies in response to the tilt angle from the 3rd to the 5th array and are incremented by the array.

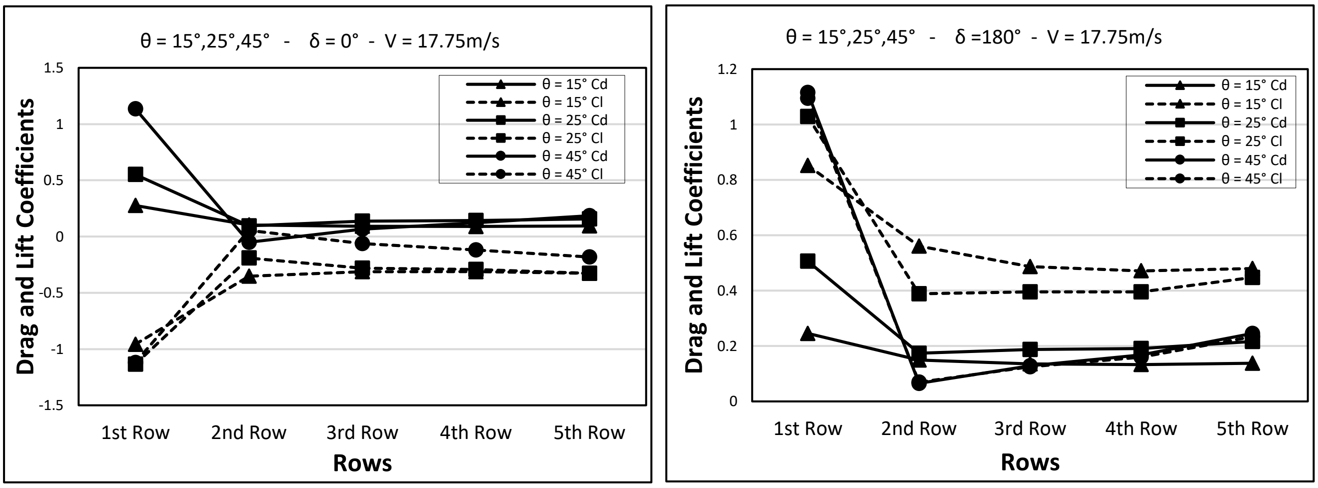

Figure 34. Drag and lift coefficients at 15°,25°, and 45° tilt angles for 0° and 180° wind directions.

5.3.2 Pressure coefficient

The pressure contours on the most affected surfaces of the panels (Upper surface for 0° and 45° wind directions and lower surface for 135° and 180° wind directions) of each array are verified to validate the results presented in the previous section. Figure 35 and Figure 36 exhibit the pressure coefficients in the range from -400 [Pa] to 190 [Pa]. Depending on the incoming flow direction, the pressure distribution at the panel edges changes.

Compared to the rest of the arrays, the pressure behavior at 0° wind direction reveals that the first row experiences a higher wind load. The leading edge of the panels has maximum coefficients, which gradually began to decrease before becoming negative at the top edge. In the following arrays, the negative pressure is dispersed over the surfaces and gets going higher from row to row. At 45° wind direction, the maximum pressure was noticed at the left corner of the panels. The first row has high coefficients due to the maximum wind load at the upper leading edge, however, the following rows show a downgrade of the pressure, particularly in the core of the panels.

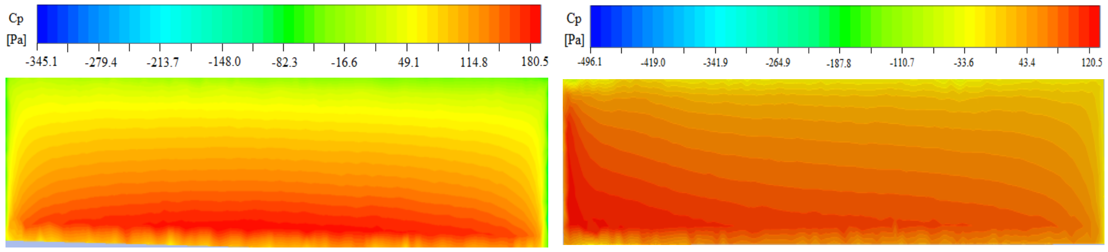

0°wind direction - 1st row 45°wind direction - 1st row

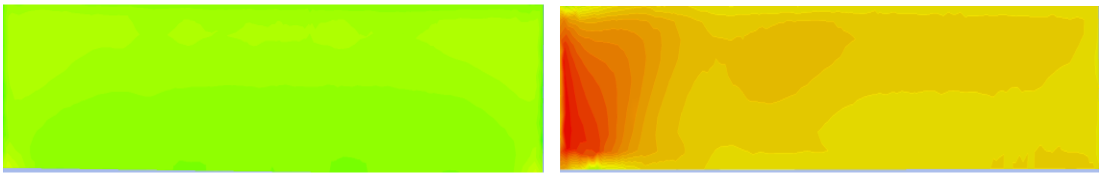

0°wind direction – 2nd row 45°wind direction – 2nd row

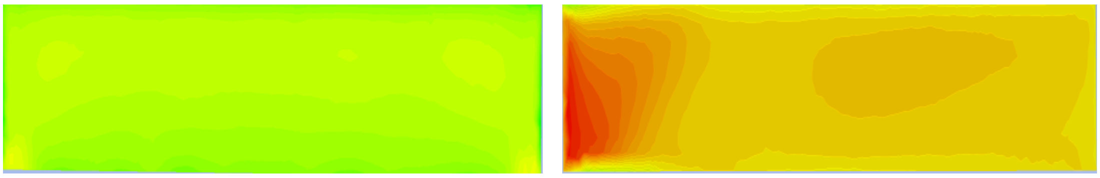

0°wind direction – 3rd row 45°wind direction – 3rd row

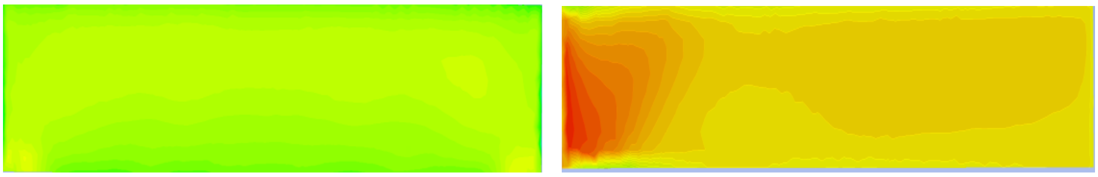

0°wind direction – 4th row 45°wind direction – 4th row

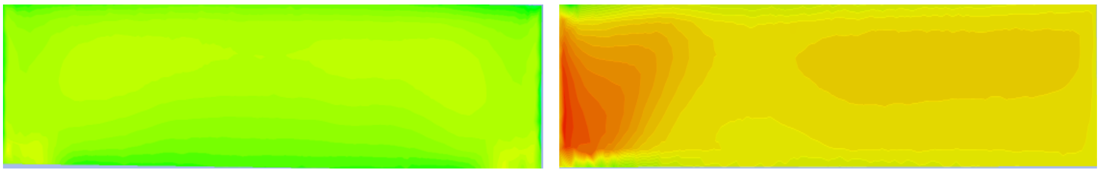

0°wind direction – 5th row 45°wind direction – 5th row

Upper Surface – 25° tilt angle

Figure 35. Pressure distribution on the upper surface at 0° and 45° wind directions.

With an inverted wind direction of 135°, a positive pressure coefficient can be seen at the upper left edge of the corner, which decreases obliquely on the surface of the 1st row, while the lower right edge shows minimal coefficient values. The mean pressure in a 180° wind direction behaves similarly to that in a 0° wind direction, although, higher pressures drop towards the lower edge and become negative at the bottom edge of the panel. The windward surface pressures ranged from -57 [Pa] to 37 [Pa] from the 2nd row to the 5th row, and the 2nd row was the most affected by the wake of the 1st row, whilst, the wind load increased from row to row.

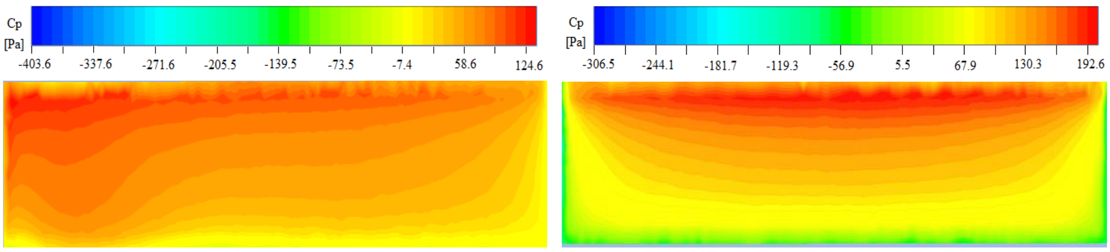

135°wind direction - 1st row

180°wind direction - 1st row

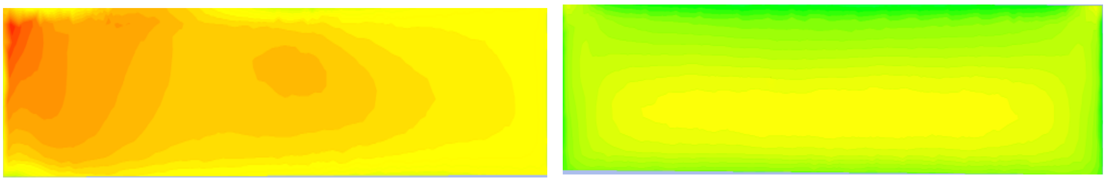

135°wind direction – 2nd row

180°wind direction – 2nd row

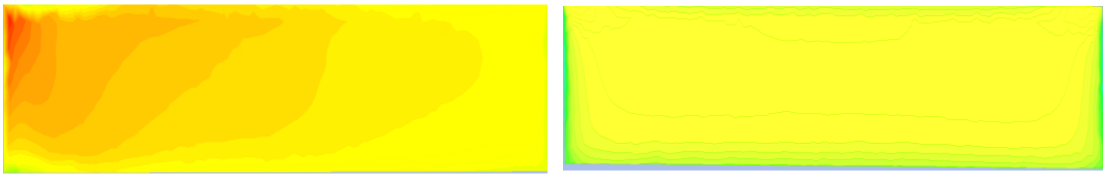

135°wind direction – 3rd row

180°wind direction – 3rd row

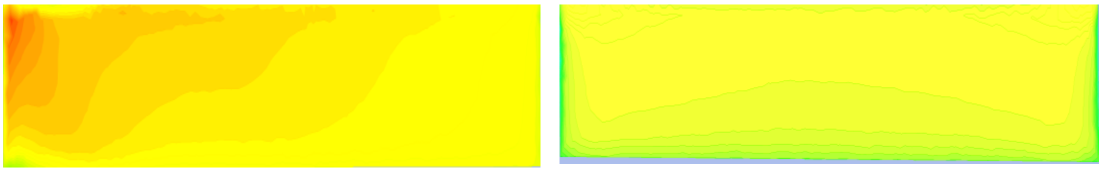

135°wind direction – 4th row

180°wind direction – 4th row

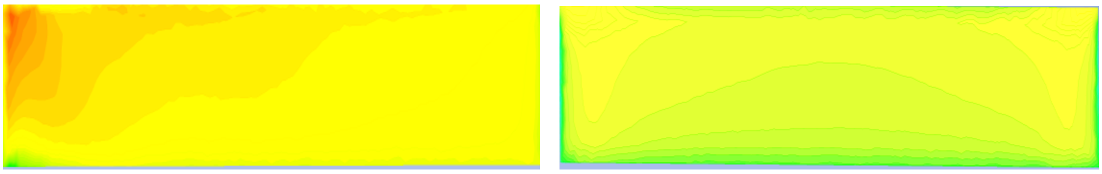

135°wind direction – 5th row

180°wind direction – 5th row

Lower Surface – 25° tilt angle

Figure 36. Pressure distribution on the lower surface at 135° and 180° wind directions.

5.4 Summary

This chapter focuses on the wind effect on five consecutive arrays separated by a distance of 1.04 H. At three different tilt angles, 15°, 25°, and 45°, the same boundary conditions were applied as for a single panel. The wind direction was computed from angles of 0°,45°,135°, and 180°.

Rows 2 to 5 experienced very low wind speed circulation in all cases, mainly at 0° and 180° wind directions, due to the wake effect of the leading row, considered the critical row of the solar plan. For reverse wind directions of 135° and 180°, the maximum wind speed was recorded around rows 2 through 5. Negative lifts were observed for 0° and 45° wind directions, whereas positive drag was observed for all wind and tilt angles. In addition, the highest wind loads for diagonal winds of 45° and 135° instead of 0° and 180° can be seen in rows 2 to 5. Regarding the pressure distribution, the lowest coefficients were found in rows 2 to 5. While the first row is under a maximum pressure on the windward surface.

The protective effect depends on the row spacing, with a reduction in the distance leading to lower aerodynamic loads on the following row, hence a smaller spacing distance is avoided by taking the row shadow into account.

Conclusion

In this study, we discussed the impact of wind loading on various solar panel configurations and the necessity to limit incidents in solar installations. Solar panels can be deployed in a variety of ways, although this thesis focuses on ground-mounted panels that can be installed in open terrain. In terms of computation time, ANSYS Fluent took about 3 hours to solve each case of our study, and both the number of elements and the type of solver affect the estimated time of the simulation. Using the RANS $k{-}\omega$ SST model, the wind was modeled as incompressible flow over a single or a series of consecutive arrays at three tilt angles (15°,25°,45°) and four wind angles (0°,45°,135°,180°). Different meshes with multiple grid sizes are evaluated and compared to (Jubayer, 2014) research for ground mounted solar panels. The mesh size has no impact on the results, although a small error percentage was observed when the number of mesh cells was increased. All chapters assumed the same boundary conditions, with atmospheric boundary layers at the inlet, zero pressure at the outlet, and a rough ground at the bottom surface.

Maximum wind loads are recorded at the leading edges of the windward surfaces for 0° and 180° wind directions, although, higher pressure is observed at the corner edges of the panel and declines obliquely for 45° and 135°.

Regarding the array’s investigation. Among the various wind directions, the first row experienced higher wind loads than the rest of the arrays, while, rows 2 to 5 had lower pressure coefficients. As the distance between modules increases, the wake zone behind the module decreases and hence the loads on arrays increase, so the front and back of the panel are also affected by spacing. In addition, the rotation of vortices changes in size and direction from one angle to the next.

The main conclusion of the current study is that the solar panels should be placed with the lowest tilt angle and the shortest spacing distances in the sake of minimizing high aerodynamic loads while considering the efficiency and optimal functionality of the solar panel. However, other parameters such as the type of ground foundation and support material can affect the cost and durability of the installation.

For future studies, it is worthwhile studying the current problem among different Reynolds numbers, as well as discussing the minimum design loads for structures as described by the American Society of Civil Engineers (ASCE).

References

Aly, A. M., & Bitsuamlak, G. (2013). Aerodynamics of ground-mounted solar panels: test model scale effects. *Journal of Wind Engineering and Industrial Aerodynamics, 123, 250-260.*

ANSYS, A. (2010). 13.0 (Release 13.0). *ANSYS Inc.*

Blocken, B., Stathopoulos, T., & Carmeliet, J. (2007). CFD simulation of the atmospheric boundary layer: wall function problems. *Atmospheric environment, 41*(2), 238-252.

BloombergNEF. (2022). Global PV installation estimate and forecast, as of January 2022. . In.

Coley, D. (2011). *Energy and climate change: creating a sustainable future*: John Wiley & Sons.

ESDU, "Characteristics of atmospheric turbulence near the ground. Part I: Definitions and general information", *ESDU International, Item No. 74030, London, 1974.*

Fluent, A. (2009). 12.1 in workbench user's guide. *ANSYS Inc., Canonsburg, PA.*

Fluent, A. (2013). ANSYS fluent theory guide 15.0. *ANSYS, Canonsburg, PA, 33.*

Foresnics, C. (2015). Solar panel modules displaced by wind forces. In.

Franke, J., Hellsten, A., Schlunzen, K. H., & Carissimo, B. (2011). The COST 732 Best Practice Guideline for CFD simulation of flows in the urban environment: a summary. *International Journal of Environment and Pollution, 44(1-4), 419-427.*

Hargreaves, D., & Wright, N. G. (2007). On the use of the k–ε model in commercial CFD software to model the neutral atmospheric boundary layer. *Journal of Wind Engineering and Industrial Aerodynamics, 95(5), 355-369.*

Jubayer, C. M. (2014). Wind and thermal effects on ground mounted photovoltaic (PV) panels.

Karimirad, M., & Moan, T. (2012). A simplified method for coupled analysis of floating offshore wind turbines. *Marine Structures, 27(1), 45-63.*

Menter, F. R. (1992). *Improved two-equation k-omega turbulence models for aerodynamic flows.*

Menter, F. R. (1997). *Eddy viscosity transport equations and their relation to the k-ε model.*

Online, C. (2014). Turbulence free-stream boundary conditions. Retrieved from https://www.cfd-online.com/Wiki/Turbulence_free-stream_boundary_conditions

Proença, M. (2018). Central Solar dos Barros, EM544, 7570, Portugal. In.

Richards, P., & Norris, S. (2011). Appropriate boundary conditions for computational wind engineering models revisited. *Journal of Wind Engineering and Industrial Aerodynamics, 99(4), 257-266.*

Shademan, M., Barron, R., Balachandar, R., & Hangan, H. (2014). Numerical simulation of wind loading on ground-mounted solar panels at different flow configurations. *Canadian Journal of Civil Engineering, 41*(8), 728-738.

Spiridonov, V., & Ćurić, M. (2021). *Fundamentals of Meteorology*: Springer.

Versteeg, H. K., & Malalasekera, W. (2007). *An introduction to computational fluid dynamics: the finite volume method*: Pearson education.

Appendix

Appendix A – UDF code for kOmegaSST

(Hargreaves & Wright, 2007)

```
#include "udf.h"
#define UREF 10.0
#define CMU 0.09
#define VKC 0.4
#define ZREF 6.0
#define Z0 0.01

DEFINE_PROFILE(velocity_profile, thread, position)
     {   float x[ND_ND];
        float y;
        float u, u_star;
        face_t f;
        u_star = UREF*VKC/log((ZREF+Z0)/Z0) ;
        begin_f_loop(f, thread)
        { F_CENTROID(x,f,thread);
          y=x[1];
          u = u_star/VKC*log((y+Z0)/Z0);
          F_PROFILE(f,thread,position) = u;
        } end_f_loop(f, thread)
     }

DEFINE_PROFILE(k_profile, thread, position)
     {   float x[ND_ND];
        face_t f;
        float u_star ;
        u_star = UREF*VKC/log((ZREF+Z0)/Z0) ;
        begin_f_loop(f, thread)
        {  F_CENTROID(x,f,thread);
          F_PROFILE(f,thread,position)=u_star*u_star/sqrt(CMU);
        }end_f_loop(f, thread)
       }

DEFINE_PROFILE(dissip_profile, thread, position)
     {   float x[ND_ND];
        face_t f;
        float u_star, y ;
        u_star = UREF*VKC/log((ZREF+Z0)/Z0) ;
        begin_f_loop(f, thread)
         {  F_CENTROID(x,f,thread);
            y=x[1];
            F_PROFILE(f,thread,position)=pow(u_star,3.)/(VKC*(y+Z0));
        }end_f_loop(f,thread)  }
```